Topological Order in String Liquids and Weyl Semimetals

by

Dan Sehayek

A thesis
presented to the University of Waterloo
in fulfillment of the
thesis requirement for the degree of
Master of Science
in
Physics

Waterloo, Ontario, Canada, 2022

Author's Declaration

This thesis consists of material all of which I authored or co-authored: see Statement of Contributions included in the thesis. This is a true copy of the thesis, including any required final revisions, as accepted by my examiners.

I understand that my thesis may be made electronically available to the public.

Statement of Contributions

Research Presented in Chapter 3

Chapter 3 contains unpublished work. In this work, I wrote all of the code pertaining to the diffusion map algorithm. The Monte Carlo data was generated using code written by Roger G. Melko, who provided a supervisory role during the course of the project.

Research Presented in Chapter 4

Chapter 4 contains research based off of [1] where I was the main author. In this work, I wrote all the code pertaining to the persistent homology algorithm using the python Ripser library [2]. The Monte Carlo data was generated using code written by Roger G. Melko, who provided an supervisory role during the course of the project.

Research Presented in Chapter 5

Section 5.4 contains research based off of [3] where I was the main author. In this work, I completed the calculations pertaining to the derivation of domain wall bound states and the nonlinear sigma model for $2Q \neq \pi$. Section 5.5 contains original, unpublished work. Anton. A. Burkov played a supervisory role during the course of both of these projects.

Abstract

Outside Landau's paradigm of symmetry-breaking orders is the class of topological orders, which cannot be described by a local order parameters. Such orders are generally defined by the presence of a gauge symmetry and possess many interesting features, including fractionalized excitations and topological degeneracy on closed manifolds. The first half of thesis will be dedicated to exploring various techniques for detecting topological order in string liquids, which are spin-1/2 systems with a local $\mathbb{Z}_2$ symmetry. Such a local symmetry gives rise to a loop condensate in the low temperature regime, which allows for emergent fractionalized excitations and topological degeneracy defined by the presence of non-contractible loops. Generally, such phases can be described by the Wegner-Wilson and 't Hooft loop observables, which are non-local string order parameters, and possess a phase transition between perimeter and area laws in spatial dimensions $D \geq 3$. We will demonstrate the ability of various numerical techniques to detect this $\mathbb{Z}_2$ topological order based on σ^z measurements sampled using a Monte Carlo algorithm for the classical $\mathbb{Z}_2$ gauge theory. First, we will show that the diffusion map algorithm can be used to cluster spin configurations according to their topological sector and hence identify the topological degeneracy for the 3-dimensional case. Next, we will show that the first Betti number of geometric complex constructions of spin configurations can be used to measure the prominence of closed loops defined by the local $\mathbb{Z}_2$ symmetry, and that a persistent homology analysis can be used to distinguish loop structures according to their geometry. We will additionally show that both the diffusion map algorithm and the first Betti number of geometric complex constructions can be used to detect the topological phase transition in the Wegner-Wilson loop between perimeter and area laws. The second half of thesis will be dedicated to exploring a construction of $\mathbb{Z}_4$ topological order in Weyl semimetals, which possess topologically protected gapless nodes hosting Weyl fermions and a chiral anomaly response. Such a construction was first proposed by C. Wang, L. Gioia and A. Burkov, and involves superconducting pairing and vortex condensation. We will show that the same $\mathbb{Z}_4$ topological can be obtained from charge density wave (CDW) interactions, which involves applying a similar vortex condensation procedure to 2D Dirac fermions at the interface between the two degenerate CDW ground states at a Weyl node separation of $2Q = \pi$. As in the original construction, fractionalized statistics will emerge in the uncondensed vortices, with odd flux vortices possessing Majorana zero modes and flux 2π vortices possessing semions. Finally, we will derive the theory of the surface states based on the hydrodynamic BF theory for this $\mathbb{Z}_4$ topological order.

Acknowledgements

During my time as a student at the University of Waterloo, I met many amazing people, many of which were my roommates and all of which are still very close friends: Stephen Brock, Kieana Fana, Atpouthan Paskaran, Akash Patel, Christopher Pollack, Ahmed Shalabi, Rane Alejandro Simpson, Karish Thangarajah, Deven Wolff, and Jacky Zhu. Whether it was learning physics together, playing intramurals together, helping each other prepare for interviews or face-planting in the hallways of the physics building, my time at Waterloo would not have been nearly as enjoyable or successful without this incredible group of people. May we continue to support each other in our academic and personal endeavors.

During my time as an undergraduate student, I add the opportunity to work with many amazing supervisors during my internships: Ray Nassar from Environment Canada, as well as Carla Barquest and Thomas Planche from Triumf. I would not be where I am today if it were not for the countless opportunities they gave me to develop as a researcher, including working on numerous projects, presenting seminars and writing conference papers. I will always be grateful for the incredibly welcoming and supportive academic environment they provided.

During my time at Triumf, I met Roger Melko, who happened to be giving an in-person seminar on machine learning for physics. Following our 10 minute discussion after the seminar, Roger Melko agreed to supervise me as a student for my remaining two undergraduate internships. Words cannot describe how grateful I am to have had Roger as a supervisor and mentor. While Roger has always had many deep and interesting insights about machine learning, quantum computing, condensed matter physics and pickle-based acronyms, he additionally provided incredible support in pursuing my own project ideas over the course my graduate degree. Roger has always made time to discuss academic and personal matters, and I always walk away from a conversation with Roger feeling more relaxed. The incredibly welcoming and motivating research environment that Roger has fostered in the PIQuIL is truly special, and want to deeply thank Roger for being my mentor over the course of my undergraduate and graduate degrees.

During my time at Perimeter Institute as an undergraduate student, I met Anton Burkov, who happened to be giving an in-person seminar on Weyl semimetals. Following our discussion, Anton agreed to supervise me for the final year PHYS 437 project, and additionally taught our classes on condensed matter physics and quantum many-body systems in the following term. Anton has always had a special talent for teaching advanced topics in a extremely well motivated manner, and truly helped deeply foster my love for

condensed matter physics and quantum field theory. The projects Anton provided me during the course of my graduate degree were natural extensions of concepts taught in these courses, which only helped further my appreciation for the field. Anton has always had the time to discuss these projects and address my questions, and I will always be incredibly grateful for having had Anton as a mentor during my time at Waterloo.

Finally, I would like to thank the amazing alumni and current students and postdocs of the PIQuIL: Michael Albergo, Matthew Beach, Stefanie Czischek, Anna Golubeva, Sofia Gonzalez, Estelle Inack, Anna Knorr, Danny Kong, Bohdan Kulchytskyy, Roger Luo, Ejaaz Merali, Schuyler Moss, Brian Timar, Isaac de Vlugt, and Sebastian Wetzel. All of these people were always willing to collaborate and have academic discussions, but at the same time were very friendly and outgoing and made my time at the PIQuIL all the more enjoyable.

Dedication

I dedicate this to my father, Rony Sehayek, who continues to be there for me in every single possible way he can, and my brother, Matthew Sehayek, who continues to inspire me in pursuing his dream.

Table of Contents

List of Figures

List of Tables

Chapter 1

Introduction

1.1 Topology in Condensed Matter

Over the past few decades, topology has continued to play an important role in the field of condensed matter. One example of this is in the band theory of solids, where topological equivalence classes of Hamiltonians are defined by continuous transformations that avoid closing the energy gap and breaking existing symmetries. Any corresponding topological invariants that are physically observable have important applications in fields such as quantum computing, due to their resilience to local perturbations of the physical system [4]. One example of such an invariant is the Landau filling factor in integer quantum Hall states, which corresponds to the total Chern number (see Section 5.2.1). Additionally, the boundaries of topological insulators and superconductors are generally characterized by symmetry-protected gapless edge states. In [5], Kitaev provides a complete framework for the classification of topological insulators and superconductors using the K-theory of vector bundles.

X. G. Wen refers to the above notion of topology as *classical topology* [6]. In essence, the term *topological* in topological insulators and superconductors really means *symmetry-protected*. On the other hand, the term *topological* in topological order generally refers to the presence of long-range entanglement. Wen refers to this notion of topology as *quantum topology*. Within Landau's theory of phase transitions, all ordered phases are described by a local symmetry-breaking order parameter, such as the magnetization order parameter in the case of ferromagnetic phases. However, beginning with the discovery of the Kosterlitz–Thouless (KT) transition of the 2D XY model [7], where the ordered phase is instead described by the binding of vortex and anti-vortex defects, it was realized that

not all ordered phases of matter are described by a local order parameter. One category of such phases is indeed the class of *topological orders*, which will be the central topic of this thesis. The defining features of topological orders are quasi-particle excitations with fractionalized statistics and topological degeneracy on closed manifolds, which generally require long-range entanglement and originate from the presence of a local symmetry [6]. Beside their theoretical intrigue, such properties have been recognized to be applicable to the development of fault-tolerant quantum computing [8, 9]. Therefore, a major effort is underway to search for and identify topologically ordered phases in materials [10], devices [11, 12], and synthetic quantum matter [13].

The challenge of detecting topological order usually involves examining the system's configuration space. Due to the lack of an order parameter, this can involve using tools such as the topological entanglement entropy [14, 15]. In situations where system configurations are represented by data, such as in computer simulations or in projective measurements of a quantum device, such tools can be prohibitively computationally expensive. This motivates the search for interpretable techniques which are inherently sensitive to topological structures in data, while remaining tractable on large finite-size lattice systems of interest to condensed matter and quantum information physics.

1.2 Outline

The outline for this thesis is as follows. In Chapter 2, we will review one of the most well known examples of topological order, namely the toric code [16]. The toric code falls under a more general class of topological orders known as quantum string liquids, which are spin-1/2 systems defined by a local $\mathbb{Z}_2$ symmetry, and refer to any such system in which the ground state wavefunction is an equal superposition over all closed string configurations [17, 6]. Generally, quantum string liquids possess topologically degenerate ground state wavefunctions which differ by the presence of non-contractible closed-strings on the torus, and two distinct quasi-particle excitations with fractionalized statistics. The order parameter defining these string liquids are the Wegner-Wilson loop and 't Hooft loops, which are non-local string operators and are invariant under the local $\mathbb{Z}_2$ symmetries, as required by Elitzur's theorem. Following this review of string liquids, Chapters 3 and 4 we will be dedicated to exploring various numerical techniques for detecting this topological order based on σ^z measurements. Specifically, we will sample spin configurations in the σ^z basis according to the classical $\mathbb{Z}_2$ gauge theory, which possesses a topological phase transition in the Wegner-Wilson loop for spatial dimensions $D \geq 3$ [18, 19].

In Chapter 3, we will show that the diffusion map algorithm [20, 21], which is a manifold

learning technique designed for clustering points according to their global connectivity, can be used to cluster spin configurations for the $D = 3$ classical $\mathbb{Z}_2$ gauge theory according to their topological sector, and hence can be used to identify the 8-fold topological degeneracy. Such an application of the diffusion map was first proposed in [22], where the same identification of topological sectors was successfully shown for the classical XY model and the classical $\mathbb{Z}_2$ gauge theory in $D = 2$. We will additionally show that ch metric, which compares the average size of the clusters to the average distance between clusters, peaks closest to the deconfinement transition, and hence can be used to identify the location of the topological phase transition. A similar idea was used [22, 23], where various clustering metrics were shown to successfully identify topological phase transitions in the XY model.

In Chapter 4, we will explore the persistent homology algorithm, which computes the significance and frequency of general loop structures in point clouds via the formation of geometric complexes [24, 25, 26, 27]. Application of the persistent homology algorithm was recently explored in the context of various symmetry-breaking and topological orders, including 1D quantum models and 2D XY models [28, 29, 30, 31, 32]. Here, Monte Carlo configurations are classified based on their persistence diagram, which contain the significance and frequency of loop structures identified in the geometric complex constructions. In our case, we will use the Vietoris-Rips (VR) complex to map Ising spin configurations from the classical $\mathbb{Z}_2$ gauge theory into geometric complexes of simplices. We will demonstrate that the resulting first Betti number can be used to measure the prominence of closed strings in the two-dimensional case and hence is largest in the topologically ordered regime, and can additionally be used to detect the topological phase transition in the three-dimensional case. This demonstrates that a full persistent homology analysis is not necessarily required to identify the phase transition. Instead, we will emphasize the persistent homology analysis as a tool for interpreting the types of loop structures that form in construction of the VR complex.

Finally, Chapter 5 will be dedicated to exploring topological order in the context of Weyl semimetals, which are characterized by topologically protected gapless nodes hosting Weyl fermions, and possess a chiral anomaly response under the presence of an electromagnetic field. We will review the model proposed by C. Wang, L. Gioia and A. Burkov [33], in which a gapped Weyl semimetal with $\mathbb{Z}_4$ topological is constructed by first adding superconducting pairing and then condensing flux 4π superconducting vortices. In this 3-dimensional model, it is the uncondensed $\Phi = n\pi$ loops for $n < 4$ that survive as gapped excitations and possess non-trivial statistics. Namely, an odd flux loop induces a Majorana zero mode upon intersection with an atomic xy plane, which implies non-Abelian statistics of loop braiding, while a $\Phi = 2\pi$ loop induces a semion upon intersection with an atomic xy plane, which implies non-trivial Abelian statistics of loop braiding. We will additionally

review the corresponding BF field theory description derived by M. Thakurathi and A. Burkov in [34].

Following this, we will show that the same $\mathbb{Z}_4$ topological order can be achieved from charge density wave interactions. To begin with, we will show that a Weyl semimetal with such interactions possesses two degenerate ground states, corresponding to two different values of phase of the charge density wave order parameter: $\varphi = 0, \pi$. We will then show that massless 2D Dirac fermions exist at the domain wall between these two degenerate ground states. Using the Hamiltonian for these domain wall bound states, we will shown that the same $\mathbb{Z}_4$ topological order as described above, namely odd flux vortices with Majorana zero modes and flux 2π vortices with semions, can be constructed following superconducting pairing and condensation of flux 4π vortices.

Finally, we will derive the edge theory of the BF theory description for this topological order. It is well known that the 2D fractional quantum Hall (FQH) liquid is described by a 2+1D Chern-Simons theory, and that the resulting edge theory is a chiral Luttinger liquid, which describes a chiral wave propagating along the boundary [35, 36]. In following the approach of X.G. Wen for the 2D FQH liquid, which involves restoring gauge-invariance by gauge-fixing on the boundary [35], we will show that the resulting 2D surface state Lagrangian for the BF theory possesses the same propagator as that of a chiral Luttinger liquid along a single direction. Ultimately, further studies of this edge theory will be left for future work.

Chapter 2

Review of $\mathbb{Z}_2$ Topological Order in String Liquids

One of the most well-known examples of topological order is the toric code, which falls under the class of general spin-1/2 string liquids [6]. The toric code is described by the following Hamiltonian [16]:

$$H = -J_z \sum_p P_p - J_x \sum_s S_s \tag{2.1}$$

where $P_p = \prod_{\ell \in p} \sigma_\ell^z$ and $S_s = \prod_{\ell \in s} \sigma_\ell^x$ are plaquette and star operators, and $\boldsymbol{\sigma}$ describes spin-1/2 degrees of freedom on the links of a periodic lattice (see Figure 2.1). In the σ_z basis, any spin configuration for which $P_p = +1$ for all p is a ground state configuration, and the transformation defined by the star operators acts as a $\mathbb{Z}_2$ gauge transformation: $[H, S_s] = 0$ with $S_s^2 = 1$. Similarly, in the σ^x basis, any spin configuration for which $S_s = +1$ for all s is a ground state configuration, and the transformation defined by the plaquette operator acts as a $\mathbb{Z}_2$ gauge transformation: $[H, P_p] = 0$ with $P_p^2 = 1$. The local symmetries defined by these gauge transformations lead to a large ground state degeneracy and ultimately long-range entanglement in the ground state wavefunctions. More specifically, the ground state wavefunctions can be understood as an equal superposition over all closed string configurations, where strings are formed over links of the direct (dual) lattice for which $\sigma^x = -1$ ($\sigma^z = -1$) (see Figure 2.2). As described in [6], this long-range entanglement can be understood as the microscopic origin for the defining features of topological order, namely quasi-particle excitations with fractionalized statistics and topological degeneracy, which will we review in the following sections.

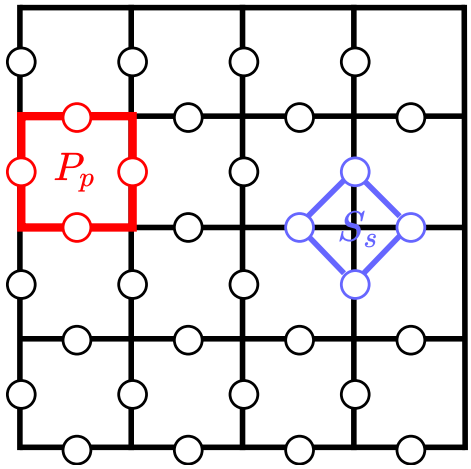

Figure 2.1: Toric code on a square lattice. Open dots represent locations of spin-1/2 degrees of freedom. The plaquette operator P_p is shown in red and the star operator S_s is shown in blue.

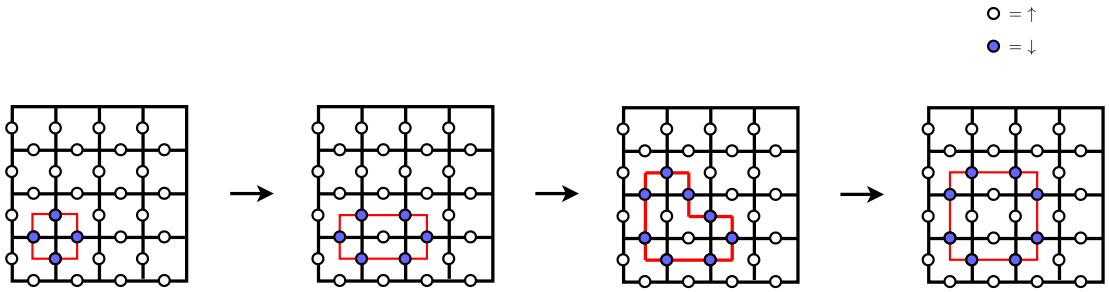

Figure 2.2: Examples of closed strings in the σ^z basis, where blue dots represent down spins. The application of a single gauge transformation to a configuration consisting solely of up spins generates a closed string of minimal size. Arrows depict steps in which single adjacent gauge transformations are applied, which stretches this loop to greater sizes. Generally, ground state configurations will consist solely of closed strings.

2.1 Anyon Excitations

In the σ^x and σ^z bases, excitations are defined by star and plaquette operators with negative parity, respectively. Such defects are generated by single spin flips are always come in pairs. It is common to refer to $S_s = -1$ excitations as electric (e) particles and $P_p = -1$ excitations as magnetic (m) particles. The reasoning behind this can be understood as follows. We begin by introducing field variables E_{ab} and A_{ab} where a and b denote sites on the lattice and ab denotes the link between sites a and b.

$$\sigma^x_{ab} = e^{iE_{ab}}$$
$$\sigma^z_{ab} = e^{iA_{ab}}$$

which implies that both E_{ab} and A_{ab} can assume values $0, \pi \pmod{2\pi}$. Expressing S_s in terms of the electric field variable:

$$\begin{aligned} S_s &= \sigma^x_{s,s+\hat{x}}\sigma^x_{s,s+\hat{y}}\sigma^x_{s,s-\hat{x}}\sigma^x_{s,s-\hat{y}} \\ &= \exp\{i\left(E_{s,s+\hat{x}} + E_{s,s+\hat{y}} + E_{s,s-\hat{x}} + E_{s,s-\hat{y}}\right)\} \\ &= \exp\{i(\mathrm{div}E)_s\} \end{aligned}$$

Since $S_s = \pm 1$, it follows that the divergence of the electric field for a given star can assume one of two values: $(\mathrm{div}E)_s = 0, \pi \pmod{2\pi}$. Hence, any given star can be viewed as having a $\mathbb{Z}_2$ charge, and the $S_s = -1$ excitation is referred to as an electric (e) particle. Similarly, we can express P_p in terms of the vector potential field variable:

$$\begin{aligned} P_p &= \sigma^z_{i,i+\hat{x}}\sigma^z_{i+\hat{x},i+\hat{x}+\hat{y}}\sigma^z_{i+\hat{x}+\hat{y},i+\hat{y}}\sigma^z_{i+\hat{y},i} \\ &= \exp\{i\left(A_{i,i+\hat{x}} + A_{i+\hat{x},i+\hat{x}+\hat{y}} + A_{i+\hat{x}+\hat{y},i+\hat{y}} + A_{i+\hat{y},i}\right)\} \\ &= \exp\{i(\nabla \times A)_p\} \\ &= \exp\{iB_p\} \end{aligned}$$

Since $P_p = \pm 1$, we see that the curl of vector potential for a given plaquette, which can be interpreted as the magnetic flux through that plaquette, can assume one of two values: $B_p = 0, \pi \pmod{2\pi}$. Hence, any given plaquette can be viewed as having a $\mathbb{Z}_2$ flux, and the $P_p = -1$ excitation is referred to as a magnetic (m) particle. The m particle is sometimes referred to as a π flux excitation or a vison.

2.1.1 Braiding

As mentioned above, quasi-particle excitations with non-trivial statistics is one of the defining features of topological order. Generally, the probabilities described by a wavefunction

$\psi(\boldsymbol{r}_1, \boldsymbol{r_2})$ for two identical particles located at $\boldsymbol{r}_1$ and $\boldsymbol{r}_2$ should remain the same upon exchange of the two particles:

$$|\psi(\boldsymbol{r}_1, \boldsymbol{r_2})|^2 = |\psi(\boldsymbol{r}_2, \boldsymbol{r_1})|^2$$

which implies $\psi(\boldsymbol{r}_1, \boldsymbol{r_2}) = e^{i\theta}\psi(\boldsymbol{r}_2, \boldsymbol{r_1})$. The cases $\theta = 0$ and $\theta = \pi$ correspond to our familiar bosons and fermions, respectively. As was first shown in [37], it turns that it is possible for particles to possess non-trivial exchange statistics $\theta \neq 0, \pi$ in the case of two spatial dimensions. Such particles are referred to as *anyons*, and have gained deep interest in the quantum computing community [9].

In the case of the toric code, the e and m particles possess trivial bosonic statistics with respect to themselves, and form a composite fermionic particle f. However, the e and m particles possess non-trivial exchange statistics $\theta = \pi/2$ with respect to each other. Namely, wrapping an e particle around an m particle induces a phase shift of π. Hence, the e and m particles are referred to as *mutual semions*. To see this, we will follow the argument from L. Balents [38], which begins by considering an initial state $|\psi_1\rangle$ containing exactly one e particle and one m particle. One can wrap the e particle around the m particle by applying a string of σ_i^z operators on a closed contour $\mathcal{C}$.

$$|\psi_2\rangle = \prod_{i \in \mathcal{C}} \sigma_i^z \, |\psi_1\rangle$$

This product of σ_i^z operators over $\mathcal{C}$ is equivalent to a product all plaquette operators contained within the region enclosed by $\mathcal{C}$:

$$\prod_{i \in \mathcal{C}} \sigma_i^z = \prod_{p \in \mathcal{A}} P_p$$

where $\mathcal{C} = \partial\mathcal{A}$. Since this enclosed region contains exactly one m particle, it follows that exactly one plaquette operator has negative parity. Hence, we find that $|\psi_2\rangle = -\,|\psi_1\rangle$ and we conclude the e and m particles are mutual semions.

As described above, the ground state wavefunction of the toric code can be understood as a superposition over all closed string configurations, with a +1 coefficient assigned to each configuration. Generally, one can obtain different non-trivial braiding statistics by modifying the rules for assigning coefficients [17, 6]. For example, if one assigns coefficients of -1 (+1) to configurations with an odd (even) number of closed strings, then the e and m particles possess semionic statistics with respect to themselves. Hence, this model is

referred to as the *double semion* model [17]. Generally, the class of $\mathbb{Z}_2$ string liquids refer to all spin-1/2 systems whose ground state wavefunctions are an equal superposition over all closed string configurations, with the braiding statistics of the quasi-particle excitations determined by the rules for assigning coefficients.

2.1.2 Fusion

Topological orders can be further classified according to the fusion rules of the anyons. Following D. Tong [36], the fusion of two anyons a and b is represented as:

$$a \star b = \sum_c N_{ab}^c c \tag{2.2}$$

where $N_{ab}^c = N_{ba}^c$ follows from $a \star b = b \star a$ and the *trivial state* 1 satisfies $a \star 1 = a$ for all a. Recall that in the case of the toric code, the e and m particles forms a composite fermionic particle f. Furthermore, we recall that the e and m particles can only be created and annihilated in pairs: flipping a single spin will always flip the parity of two plaquettes. For this reason, the toric code and general string liquids are referred to as having a $\mathbb{Z}_2$ topological order. Ultimately, the fusion rules for the toric code are as follows:

$$\begin{array}{lll} 1 \star e = e & 1 \star m = m & 1 \star f = f \\ e \star m = f & e \star f = m & m \star f = e \\ e \star e = 1 & m \star m = 1 & f \star f = 1 \end{array}$$

2.2 Topological Degeneracy

Recall that the toric code and general spin-1/2 string liquids are defined on a periodic lattice. Hence, it is possible to have closed strings that are non-contractible. Generally, there are two topologically distinct families of non-contractible loops on a torus, which cannot be smoothly deformed into each other (see Figure 2.3). Generating a single non-contractible loop in a ground state configuration requires applying a string of spin flips, such that the pair of e or m particles generated upon the first spin flip eventually meet and annihilate. Ultimately, ground state configurations differing by the presence of a non-trivial string are said to belong to different *topological sectors* and are restricted to their topological sector at sufficiently low temperatures and sufficiently large system sizes, since non-trivial strings cannot be generated or removed using gauge transformations. Since there are two topologically distinct families of non-trivial loops, there are four distinct topological sectors, and

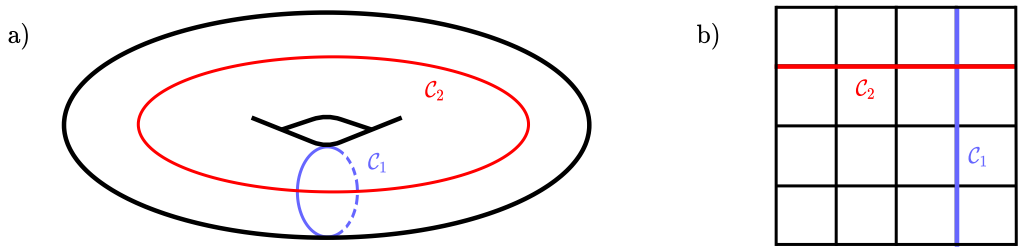

Figure 2.3: Examples of topologically distinct non-trivial contours $\mathcal{C}_1$ and $\mathcal{C}_2$ on the torus.

hence four topologically distinct ground state wavefunctions. Since this degeneracy is due to the topology of the torus, it is commonly referred to as *topological degeneracy*. Note that adding multiple non-trivial strings does not define additional sectors, since pairs of non-trivial strings of the same kind can be eliminated via gauge transformations.

2.3 Higher Form Symmetry

Another general feature of topological orders is the presence of *higher form symmetries* [39, 40]. In fact, higher form symmetries can be understood as the mechanism for topological order. Recall that in the context of the toric code and general string liquids, the plaquette and star operators act as symmetry operators in the σ^x and σ^z bases. The presence of such local symmetries forbids the presence of a local order parameter by Elitzur's theorem [41]. Intuitively, any observable that does not possess invariance under these local symmetries will tend to zero due to gauge fluctuations. In the context of string liquids, the only gauge-invariant observables are the Wegner-Wilson loop and 't Hooft loop observables, which are defined as:

$$W_{\mathcal{C}} = \prod_{\ell \in \mathcal{C}} \sigma^z_\ell \tag{2.3}$$

$$V_{\tilde{\mathcal{C}}} = \prod_{\ell \in \tilde{\mathcal{C}}} \sigma^x_\ell \tag{2.4}$$

where $\mathcal{C}$ and $\tilde{\mathcal{C}}$ define closed contours on the direct and dual lattices, respectively (see Figure 2.4 for examples). The Wegner-Wilson loop acts as the most general gauge transformation for spin configurations in the σ^x basis, with $W_{\mathcal{C}}$ for the smallest contour corresponding to a plaquette. Similarly, the 't Hooft loop acts as the most general gauge transformation for spin configurations in the σ^z basis, with $V_{\tilde{\mathcal{C}}}$ for the smallest contour corresponding

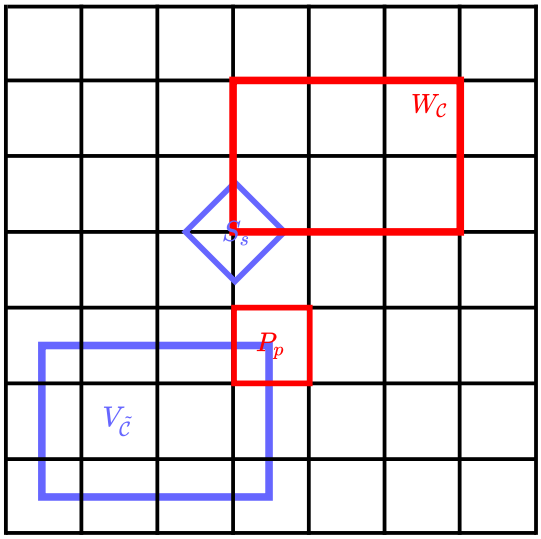

Figure 2.4: Examples of the Wegner-Wilson loop and 't Hooft loop observables. Any Wegner-Wilson loop acts as a symmetry operator for the toric code in the σ^x basis, since it intersects any star operator an even number of times, and hence leaves the parities of all the star operators unchanged. Similarly, any 't Hooft loop acts as a symmetry operator for the toric code in the σ^z basis, since it intersects any plaquette operator an even number of times, and hence leaves the parities of all the plaquette operators unchanged.

to a star. Since these symmetry operators are defined in terms of 1-dimensional strings of Pauli operators, they are referred to as *1-form symmetries* [42]. In the topologically ordered phase, $\langle W_{\mathcal{C}} \rangle$ and $\langle V_{\tilde{\mathcal{C}}} \rangle$ are non-zero due to invariance with respect to the 1-form symmetries, and go to zero upon condensation of m and e particles, respectively.

The string operators $W_{\mathcal{C}}$ and $V_{\tilde{\mathcal{C}}}$ can also be used to determine the topological sector of ground states. Namely, if $\mathcal{C}_1$ belongs to the family of non-trivial loops of the first kind, then $W_{\mathcal{C}_1} = -1$ implies the existence of an odd number of non-trivial closed strings of the second kind. This holds since all trivial closed strings must intersect $\mathcal{C}_1$ an even number of times, while all non-trivial closed strings of the second kind must intersect $\mathcal{C}_1$ an odd number of times. Similarly, if $\mathcal{C}_2$ belongs to the family of non-trivial loops of the second kind, then $W_{\mathcal{C}_2} = -1$ implies the exist of an odd number of non-trivial closed strings of the first kind. Hence, $W_{\mathcal{C}_1}$ and $W_{\mathcal{C}_2}$ collectively determine the topological sector of a ground state configuration in the σ^z basis. If one enters the topologically ordered phase upon the confinement of m particles, then $\langle W_{\mathcal{C}_\alpha} \rangle$ will transition from zero to ± 1. This can be understood as a *higher-form symmetry breaking*, with the symmetry breaking in the case

corresponding to the selection of a topological sector. Such a topological phase transition can be driven with the presence of an external field term $h_x \sum_\ell \sigma^x_\ell$. Namely, one can show that there exists a critical value of the external field at which the Wegner-Wilson loop transforms between perimeter and area laws [18, 19, 43]:

$$\langle W_{\mathcal{C}} \rangle \sim \exp(-\alpha(T) P_{\mathcal{C}}) \tag{2.5}$$

$$\langle W_{\mathcal{C}} \rangle \sim \exp(-\beta(T) A_{\mathcal{C}}) \tag{2.6}$$

where $P_{\mathcal{C}}$ and $A_{\mathcal{C}}$ are the perimeter and area of the closed contour $\mathcal{C}$. Namely, $P_{\mathcal{C}}$ refers to the number of links contained in $\mathcal{C}$, while $A_{\mathcal{C}}$ refers to the number of plaquettes contained within $\mathcal{C}$. Here, the phase where $W_{\mathcal{C}}$ obeys a perimeter law corresponds to the topologically ordered phase where $\mathbb{Z}_2$ flux is expelled, and the area law corresponds to the disordered phase where $\mathbb{Z}_2$ flux proliferates. An analogous discussion can be made for the 't Hooft loop in the σ^x basis.

Finally, we note that if one instead considers open strings $\mathcal{L}$ and $\tilde{\mathcal{L}}$ on the direct and dual lattices, then the loop observables become generators of the quasi-particle excitations. Namely, $W_{\mathcal{L}}$ generates a pair of e particles upon application to a ground state configuration in the σ^x basis, with each end of the open string containing one e particle. Similarly, $V_{\tilde{\mathcal{L}}}$ generates a pair of m particles upon application to a ground state configuration in the σ^z basis, with each end of the open string containing one m particle.

Chapter 3

Detecting Topological Order with Manifold Learning

As discussed in Chapter 2, both non-trivial braiding statistics of the quasi-particle excitations and topological degeneracy on closed manifolds are defining features of topological order, and ultimately originate from local $\mathbb{Z}_2$ symmetries in the case of general string liquids. In Chapters 3 and 4, we will exploit various numerical techniques based on geometry and topology to identify the topological degeneracy, closed loop structures and higher-form symmetry breaking resulting from the local $\mathbb{Z}_2$ symmetry defined by S_s. We will sample spin configurations in the σ^z basis according to the classical $\mathbb{Z}_2$ gauge theory [19, 18]:

$$H = -J_z \sum_p P_p \tag{3.1}$$

where $P_p = \prod_{\ell \in p} \sigma^z_\ell$ are the plaquette operators as defined in the toric code. Specifically, we employ a standard classical Monte Carlo method consisting of cluster updates ($\mathbb{Z}_2$ gauge transformations) and local updates (spin flips) to sample spin configurations according to the Metropolis algorithm. Following a standard Peierls argument, the classical $\mathbb{Z}_2$ gauge theory described by Equation 3.1 can be shown to possess a perimeter to area law transition in the Wegner-Wilson loop for $D \geq 3$ [19, 18, 44].

In this chapter, we will explore the application of a manifold learning algorithm, namely the diffusion map [20, 21], to the classification of Monte Carlo configurations based on their topological sector, and hence the identification of the topological degeneracy. This concept was first proposed in [22], where the diffusion map was shown to be successful in sector

classification in the context of the classical XY model and the pure classical $\mathbb{Z}_2$ gauge theory in $D = 2$. Standard clustering metrics were then shown to be successful in identifying the location of the vortex-antivortex deconfinement transition in the case of the $2D$ XY model. We will investigate the ability of the diffusion map to identify the 8-fold topological degeneracy in the $3D$ pure classical $\mathbb{Z}_2$ gauge theory, as well as the deconfinement transition of the Wegner-Wilson loop. To begin, we will introduce the diffusion map algorithm.

3.1 The Diffusion Map Algorithm

A fundamental object in unsupervised clustering algorithms is the kernel matrix, which measures local similarity between points in a feature space. If $\boldsymbol{x}_\alpha = \left(x_\alpha^1, ..., x_\alpha^D\right)$ represents a single point α in a D-dimensional feature space, then the kernel matrix comparing two points x_α and x_β is denoted $K(x_\alpha, x_\beta)$. It assumes a value of 1 if the points are identical and tends to zero as the distance between the points tend to infinity. One of the most commonly used kernel matrices is the Gaussian kernel:

$$K(x_\alpha, x_\beta) = \exp\left(-\frac{|x_\alpha - x_\beta|^2}{\epsilon}\right) \tag{3.2}$$

where ϵ is the size of the kernel. Namely, two points with a fixed distance of separation will generally have smaller similarity for smaller ϵ. In standard clustering algorithms, two points with a larger value of $K(x_\alpha, x_\beta)$ are more likely to be identified as belonging to the same category. We notice however, that such a notion is not effective for clustering points based on global connectivity. Namely, the kernel contains no information about global connectivity between points in the feature space. There does however exist a class of clustering algorithms called *manifold learning* algorithms that are precisely designed to cluster data based on global connectivity [45], and one example of this is the diffusion map [20, 21]. While the kernel matrix does not possess any information about global connectivity, it serves as an important first step in the diffusion map algorithm. We begin by normalizing the kernel matrix as follows:

$$P_{\alpha\beta} = \frac{K(x_\alpha, x_\beta)}{z_\alpha} \tag{3.3}$$

where $z_\alpha = \sum_\ell K(x_\alpha, x_\ell)$ and $P_{\alpha\beta}$ is referred to as the *diffusion matrix*. With this normalization, $P_{\alpha\beta}$ can be interpreted as the probability of moving from point α to point β in a single time step of a random walk. The essence of the diffusion map is to then integrate

these local connectivities to determine global connectivities: $P^t_{\alpha\beta}$ can be interpreted as the probability of moving from point α to point β after t time steps. For example, if two data points are present, then $P^2_{11} = p_{11}p_{11} + p_{12}p_{21}$. The first term is the probability of remaining stationary after two time steps, while the second term is the probability of moving from 1 to 2 in the first time step and then from 2 back to 1 in the second time step. Ultimately, one can then formulate a global connectivity metric using this diffusion matrix.

$$D_t(x_\alpha, x_\beta) = \sqrt{\sum_\ell \left| P^t_{\alpha\ell} - P^t_{\ell\beta} \right|^2} \tag{3.4}$$

This is called the *diffusion distance*. Namely, two points with high global connectivity will have a small diffusion distance, while two points with low global connectivity will have a large diffusion distance. To see this, note that $\left| P^t_{\alpha\ell} - P^t_{\ell\beta} \right|$ makes a large contribution for any point ℓ that is globally connected to solely α or β. While this metric is effective at computing global connectivity, it quickly becomes intractable. To circumvent this issue, one can alternatively map the data to diffusion space by diagonalizing the diffusion matrix. Namely, if the diffusion matrix possesses k eigenvalues and eigenvectors $\{\lambda_i, \boldsymbol{\psi}_i\}$, then the mapping of a given data point x_α to diffusion space is given by:

$$\Psi(x_\alpha) = \begin{bmatrix} \lambda_1 \psi_1(x_\alpha) \\ \vdots \\ \lambda_k \psi_k(x_\alpha) \end{bmatrix} \tag{3.5}$$

where $\psi_i(x_\alpha)$ refers to component α of eigenvector $\boldsymbol{\psi}_i$. Namely, for each data point x, there exists one diffusion coordinate for each of the k eigenvectors, with more significant coordinates corresponding to larger eigenvalues. Following [21], one can show that the Euclidean distance in this diffusion space is the diffusion distance in the original Euclidean space. With this mapping, one can finally use a simple k-means algorithm to identify clusters based on global connectivity. Figure 3.1 shows a simple example, where a diffusion map is applied to a set of data points, where each data point can clearly be associated with one of two manifolds: a circle of radius $r = 1$ and a circle of radius $r = 10$. Upon mapping the data to diffusion space, these global clusters become local clusters. In this case, the diffusion coordinate with the largest eigenvalue is sufficient for distinguishing the two global clusters, and can be viewed as measuring the radius of any given point. With this, we see that the diffusion map also serves as a *dimensionality reduction* technique. Namely, only the diffusion coordinates with the largest eigenvalues are necessary for distinguishing the global clusters of points. In this case, while the points live a 2-dimensional feature space,

the diffusion map successfully identifies that only one coordinate is required to distinguish the two manifolds, namely the radius coordinate r.

3.2 Detecting Topological Degeneracy

As discussed in Section 2.2, the toric code possesses topological sectors defined by the presence non-trivial loops of $\downarrow$ spins on the torus. The results in distinct topological sectors and hence a topological degeneracy of the ground state wavefunction for the toric code. As discussed in Section 2.3, the topological sector to which a given ground state configuration belongs is generally determined by the sign of the Wegner-Wilson loop observables $W_{\mathcal{C}_\alpha}$, where $\mathcal{C}_\alpha$ represent non-trivial contours on the torus. In the $D = 3$ case, there are three distinct non-trivial contours, and hence 8 unique topological sectors. In this section, our goal is to identify this topological degeneracy by clustering spin configurations according to their topological sector. Namely, we will use the manifold learning algorithm described above to identify a unique manifold in configuration space for each topological sector. To use any clustering algorithm, we require a metric for comparing spin configurations. The most obvious choice is the standard Euclidean metric:

$$d^2(\boldsymbol{\sigma}_\alpha, \boldsymbol{\sigma}_\beta) = \frac{1}{N} \sum_\ell \left(\sigma^z_{\alpha,\ell} - \sigma^z_{\beta,\ell}\right)^2 \tag{3.6}$$

where $\boldsymbol{\sigma}_\alpha$ represents a single Monte Carlo configuration and ℓ labels one of $N = 3 \times L^3$ links on the lattice. This however is insufficient for our problem, as it fails to consider the local $\mathbb{Z}_2$ symmetry of the model. As an example, any two ground states that are equivalent under a global $\mathbb{Z}_2$ transformation belong to the same topological sector for even L, but would have maximal separation and minimal similarity under this Euclidean metric. Ideally, ground state configurations belonging to the same topological sector should have zero distance and maximal similarity, if our goal is to identify unique manifolds in configuration space for each topological sector.

As discussed above, the star operator S_s is the generator of the local $\mathbb{Z}_2$ symmetry of the classical $\mathbb{Z}_2$ gauge theory. This implies that any two ground state configurations $\boldsymbol{\sigma}_1$ and $\boldsymbol{\sigma}_2$ belonging to the same topological sector are equivalent via gauge transformations. More precisely, one can always find a string of gauge transformations $S_{s_1} \cdots S_{s_n}$ such that $\boldsymbol{\sigma}_1 = S_{s_1} \cdots S_{s_n} \boldsymbol{\sigma}_2$. This is no longer the case for two ground states belonging to different topological sectors, since generating a non-trivial string requires applying a string of local spin flips of the linear size of the lattice. Motivated by this, we consider a modification

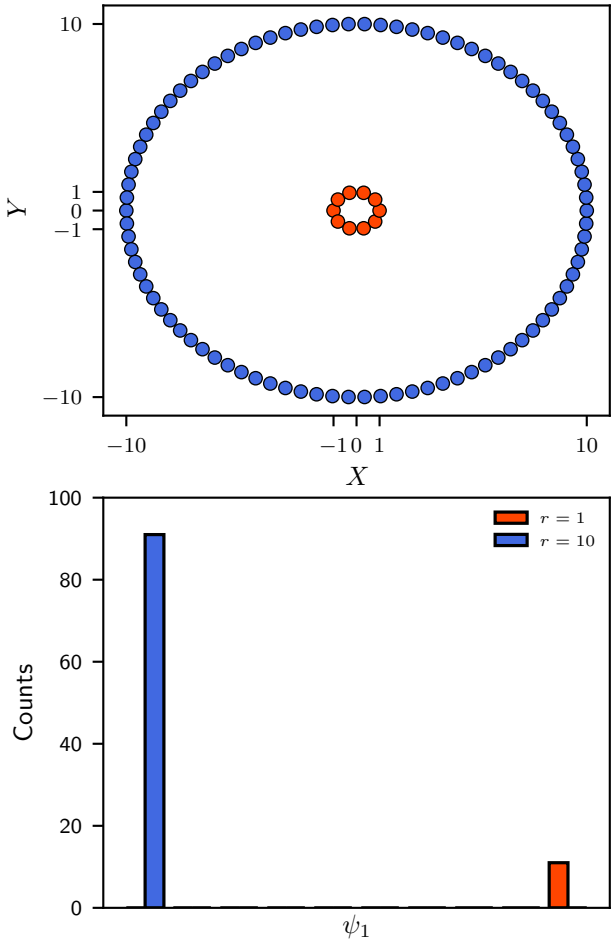

Figure 3.1: Top: Set of data points. Each data point can clearly be associated with one of two distinct manifolds: a circle of radius $r = 1$ (shaded red) and a circle of radius $r = 10$ (shaded blue). Bottom: Histogram of first diffusion map coordinate for circle data. Ultimately, we see that the global clusters in the original space become local clusters in the diffusion space. In this case, one diffusion map coordinate is clearly sufficient for distinguishing the two global clusters.

of the Euclidean metric that involves a preliminary *gauge-matching* step, which was first proposed in [22] for the $D = 2$ case. Namely, for any two spin configurations $\boldsymbol{\sigma}_\alpha$ and $\boldsymbol{\sigma}_\beta$, we generate a random sequence of sites $\{\boldsymbol{r}_i\}_{i=1}^{N_G}$ on the lattice. At each step i, one can compute $\boldsymbol{\sigma}'_a = G(\boldsymbol{r}_i)\boldsymbol{\sigma}_a$ and *accept* the gauge transformation only if $d(\boldsymbol{\sigma}'_a, \boldsymbol{\sigma}_b) \leq d(\boldsymbol{\sigma}_a, \boldsymbol{\sigma}_b)$ for the standard Euclidean metric defined in Equation 3.6.

Our goal then is to implement the diffusion map algorithm described above using the Euclidean metric with this preliminary gauge-matching step. Specifically, we apply this algorithm on spin configurations generated using a Metropolis sampling of Equation 3.1. For a given temperature, 8 separate Monte Carlo routines are executed, with the initial configurations of these routines belonging to distinct topological sectors from each other, so as to allow for the formation of all possible sector manifolds. For a single Monte Carlo routine and a sufficiently low temperature, such that no local spin flips are applied, the system will remain in the topological sector of the initial configuration. Assuming a sufficient number of proposals, all spin configurations in this routine will have zero distance with respect to each other and hence belong to the same point in configuration space under the metric defined above. As the temperature is increased, spin configurations with vison defects will begin to appear, and points in configuration space with steadily increasing distances from the point representing ground state configurations will begin to form. Ultimately, this defines a sector manifold, and there exists one of these distinct manifolds for each topological sector, as is shown in Figure 3.2 for the $D = 3$ case. We additionally see that the sector manifold to which a given spin configuration belongs can be determined by the averaged Wegner-Wilson loop:

$$\bar{W}_\alpha = \frac{1}{N} \sum W_\alpha^{(i)} \tag{3.7}$$

where N is the linear size of the lattice. The sign of $\bar{W}_\alpha$ can be interpreted as the *proximal sector*, and the value can be interpreted as the closeness to this sector, where $\bar{W}_\alpha = 0$ indicates that the given configuration cannot be uniquely associated to any given sector. As the temperature is increased, vison pairs or open strings become more prominent, and $\bar{W}_\alpha = 0$ becomes more likely.

3.3 Detecting Deconfinement

As was shown in [22, 23], the diffusion map algorithm can additionally be used to identify topological phase transitions, which in our case is the perimeter to area law transition in the Wegner-Wilson loop. Generally, one expects that as the temperature is increased,

these sector manifolds expand and eventually merge, since proliferation of vison defects would allow for the formation or elimination of non-trivial strings and hence would allow for hopping between sectors. The idea proposed and successfully implemented in [22, 23] is to use the point at which a standard classification algorithm is no longer able to distinguish these sector manifolds as a signal for the topological phase transition. Following the mapping of spin configurations to diffusion space, we follow the approach of [23] and compute a k-means clustering metric known as the Calinski-Harabasz (ch) index for each ensemble of spin configurations at the temperatures considered. Essentially, the k-means clustering will attempt to assign each spin configuration to one of k clusters or categories. The ch index then compares the average inter-cluster distance to the average size of the clusters. Values of the ch index for various temperatures are shown in Figure 3.3. As is found in [23], we find that the ch metric is largest close to the critical point, which in our case is located at a critical temperature of $T_c = 1.314$.

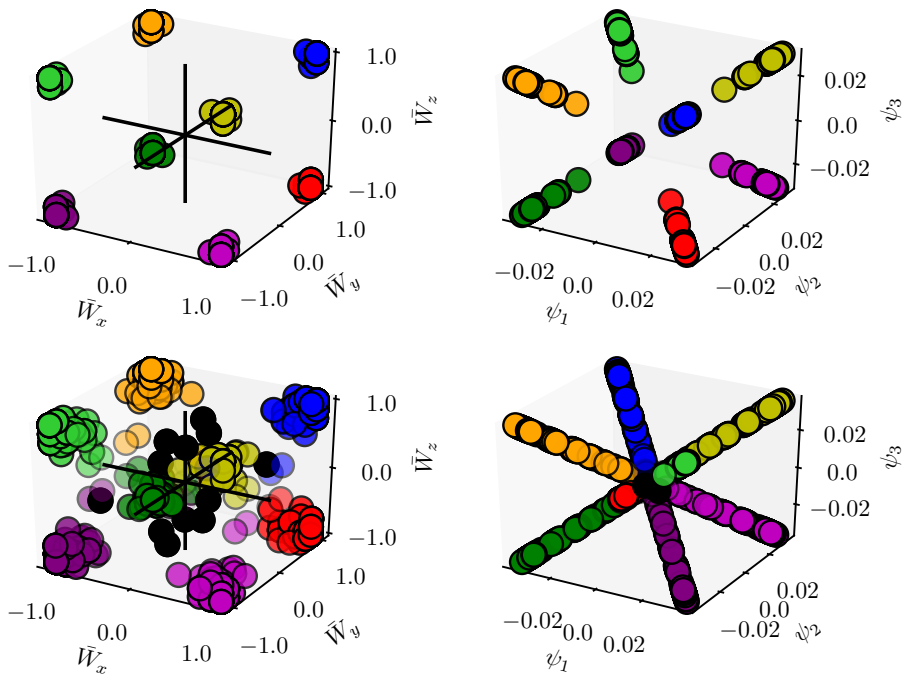

Figure 3.2: Left: Average Wegner-Wilson loop observables of Ising configurations generated from a Monte Carlo for the classical $\mathbb{Z}_2$ gauge theory in $D = 3$ with cluster updates. Eight independent Monte Carlo runs are executed, each with an initial state corresponding to a different topological sector. 160 samples are generated in each run. Black dots correspond to samples with $\bar{W}_\alpha = 0$. Right: Diffusion map construction for Monte Carlo samples. Top and bottom plots correspond to $T = 0.9$ and $T = 1.3$ respectively.

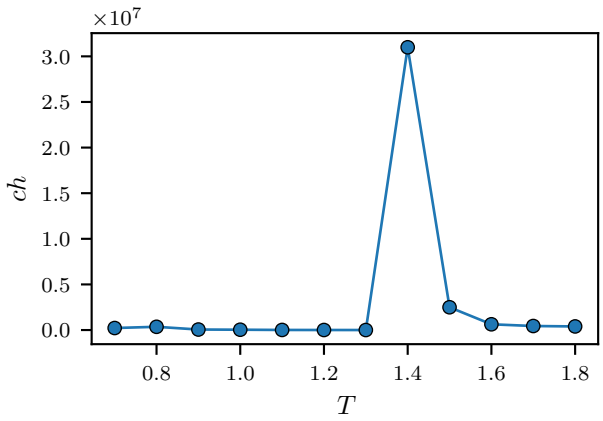

Figure 3.3: Following the mapping of Ising configurations for the classical $\mathbb{Z}_2$ gauge theory to diffusion space, a k-means clustering is applied and the ch metric is computed for each temperature. As was observed in [23] for various XY models, there exists a peak in the ch index close to the critical temperature.

Chapter 4

Detecting Topological Order with Persistent Homology

In Chapter 3, we demonstrated the ability of the diffusion map algorithm to identify the topological degeneracy and detect the topological phase transition in the $\mathbb{Z}_2$ gauge theory. In this chapter, we will explore another framework for studying the topological order of the $\mathbb{Z}_2$ gauge theory, which will focus on studying the topology of geometric complexes constructed from Ising spin configurations. This concept has already been explored in the context of 1D quantum models, 2D XY models and the 3D XXZ model [29, 30, 31, 32]. In these papers, machine learning algorithms are used to classify spin configurations and hence construct phase diagrams according to their persistence diagrams, which encode the size and frequency of loop structures resulting from their geometric complex constructions. The framework for identifying and distinguishing these loop structures is referred to as *persistent homology*, which we will introduce below.

In this chapter, our goal will be to identify the closed loop structures resulting from the local $\mathbb{Z}_2$ symmetry using the Vietoris-Rips (VR) complex construction, which can be understood as a mapping of Ising configurations to a simplicial complex, and will be introduced below. Upon this construction, we will show that the resulting first Betti number is largest in the topologically ordered regime, where loops are condensed. We will additionally show that this first Betti number successfully identifies the deconfinement transition in the $D = 3$ case. This work will be unlike the work done in [29, 30, 31, 32] in that the persistent homology analysis will not be used to construct persistence diagrams for machine learning classification, and will instead simply be emphasized as a tool for interpreting the types of loop structures that form in the construction of the VR complexes.

Before discussing this framework, we will begin with a review of fundamental concepts in algebraic topology.

4.1 Review of Algebraic Topology

Topology is concerned with global properties of shapes: properties that remain unchanged under smooth transformations that avoid cutting and pasting. If such a transformation exists between two objects, then the two objects are regarded as *topologically equivalent*. In this section, we will first introduce the concept of homotopy, which will make the notion of topological equivalence more clearly defined. Following this, we will review homology and the notion of simplices, which provide a framework for computing homotopy. Finally, we we will review the Vietoris-Rips complex, which is a formalism for detecting loop structures and ultimately assigning topologies to point clouds (0-dimensional manifolds).

4.1.1 Homotopy

Homotopy provides a rigorous formalism for establishing topological equivalence between objects, and is based on the notion of equivalence classes of loops. We say that any two loops $\gamma_1(t)$ and $\gamma_2(t)$ defined on a manifold $\mathcal{M}$ belong to the same *homotopy class* if there exists a continuous function $H(t, s)$ on $\mathcal{M}$ such that $H(t, 0) = \gamma_1(t)$ and $H(t, 1) = \gamma_2(t)$. As examples, we consider the two manifolds shown in Figure 4.1, where $\mathcal{B}$ differs from $\mathcal{A}$ by the presence of a hole. One can draw infinitely many loops on $\mathcal{A}$, but all such loops can be continuously deformed into each other. Since all possible loops on $\mathcal{A}$ are contractible to a single point, their respective homotopy class is labelled the *trivial class*.

Now consider $\mathcal{B}$. Any loop that encloses the hole is not contractible to a single point, and hence belongs to a nontrivial class. Since loops are allowed to self-intersect, there exists a new nontrivial class for each winding number around the hole. The set of all homotopy classes for a given manifold can be used to form a group, where the trivial class is the identity element and the group operation is the addition of loops. For example, adding two loops of winding numbers m and n forms a loop of winding number $m + n$. Such a group of a manifold $\mathcal{M}$ is called the *homotopy group* of $\mathcal{M}$ or $\pi_1(\mathcal{M})$. Since the homotopy group of $\mathcal{A}$ consists solely of the trivial class, $\pi_1(\mathcal{A}) \cong 0$. Since the homotopy group of $\mathcal{B}$ consists of an additional homotopy class for each winding number $n \in \mathbb{Z}$, $\pi_1(\mathcal{B}) \cong \mathbb{Z}$.

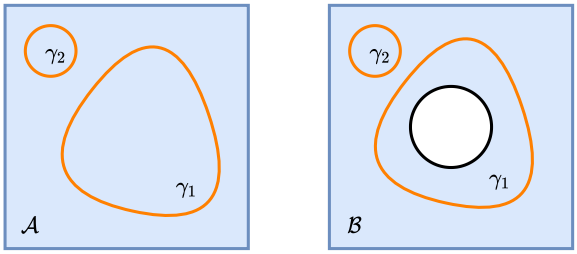

Figure 4.1: Two manifolds $\mathcal{A}$ and $\mathcal{B}$ and two curves γ_1 and γ_2. In $\mathcal{A}$, γ_1 and γ_2 are homotopically equivalent, since they can be smoothly deformed into each other. However, in $\mathcal{B}$, γ_1 and γ_2 are not homotopically equivalent, since γ_2 winds around a hole while γ_1 does not. Generally, there exists a homotopy class for each winding number around any given hole.

The subscript in π_1 refers to the fact that 1-dimensional loops are used to construct homotopy classes. π_1 is called the first homotopy group or the fundamental group. It is possible to construct higher order homotopy groups from n-loops, these are denoted π_n. Higher order homotopy groups are necessary for detecting higher dimensional holes. For example, consider the circle S^1 and the sphere S^2. 1-loops are capable of detecting the hole in S^1, and ultimately $\pi_1(S^1) \cong \mathbb{Z}$ following the same line of reasoning as above. However, 1-loops are not capable of detecting the higher dimensional hole in S^2: all 1-loops on the surface of a hollow sphere are contractible to a single point. Hence, $\pi_1(S^2) \cong 0$. Instead, one can use 2-loops (two-dimensional closed surfaces). In analogy with the discussion above, there exists a homotopy class of 2-loops for each winding number around the 3-dimensional hole. Hence, $\pi_2(S^2) \cong \mathbb{Z}$.

Generally, a manifold $\mathcal{M}$ with m holes of dimension n has a homotopy group $\pi_{n-1}(\mathcal{M}) = \mathbb{Z} \oplus \cdots \oplus \mathbb{Z} \equiv \mathbb{Z}^m$, since a set of nontrivial winding classes exists for each hole. Ultimately, these homotopy groups allow for a rigorous notion of topological equivalence. Namely, two objects $\mathcal{A}$ and $\mathcal{B}$ are topologically equivalent if $\pi_n(\mathcal{A}) \cong \pi_n(\mathcal{B})$ for all n. One can additionally define a set of topological invariants known as the *Betti numbers*, where the n^{th} Betti number of a manifold $\mathcal{M}$, denoted b_n, corresponds to the number of $n+1$ dimensional holes of $\mathcal{M}$, and is given by the rank of the n^{th} homotopy group:

$$b_n(\mathcal{M}) = \text{rank}\left(\pi_n(\mathcal{M})\right) \tag{4.1}$$

Namely, if $\pi_n(\mathcal{M}) = \mathbb{Z}^m$ then $b_n(\mathcal{M}) = m$.

4.1.2 Homology

Homology is a framework for computing homotopy. To begin with, let us consider a general graph X constructed from cells. Generally, an n-cell is an n-dimensional object, and the boundaries of an n-cell are $n-1$ cells. For example, a 0-cell is a point, a 1-cell is a directed line, and a 2-cell is a oriented disk. Any combination of n-cells is then referred to as n-chain of the graph X. If C_n denotes the set of all n-chains of a graph X, and ∂_n is the boundary operator of n-chains, it follows that $\partial_n : C_n \to C_{n-1}$. The n^{th} homotopy group of the graph X can then be computed via the n^{th} homology group of X:

$$H_n(X) = \frac{Z_n(X)}{B_n(X)} = \frac{\ker(\partial_n)}{\text{im}(\partial_{n+1})} \tag{4.2}$$

where $Z_n(X) = \ker(\partial_n)$ refers to the n-dimensional cycles of X (called n-cycles) and $B_n(X) = \text{im}(\partial_{n+1})$ refers to n-dimensional boundaries of X (called n-boundaries). To understand the motivation behind this, we consider the two graphs shown in Figure 4.2. Both graphs possess the same 0-chains and 1-chains, where 0-cells and 1-cells are labelled by greek and roman letters respectively. However, graph $\mathcal{B}$ possesses an additional 2-cell labelled by A. The boundaries of each of the 1-cells are as follows:

$$\begin{aligned}
\partial_1(a) &= \alpha - \gamma \\
\partial_1(b) &= \beta - \alpha \\
\partial_1(c) &= \gamma - \beta \\
\partial_1(d) &= \delta - \beta \\
\partial_1(e) &= \gamma - \delta
\end{aligned}$$

Any 1-cycle satisfies $\partial_1 = 0$. For example, $a+b+c$ forms a 1-cycle, since $\partial_1(a+b+c) = 0$. To determine all 1-cycles, one can then solve $\partial_1(n_1a+n_2b+n_3c+n_4d+n_5e) = 0$ where $n_i \in \mathbb{Z}$, which yields a system of linear equations. This gives $\ker \partial_1 = \langle a+b+c, a+b+d+e \rangle \cong \mathbb{Z} \oplus \mathbb{Z} \equiv \mathbb{Z}^2$, implying their are 2 independent cycles. Since there are no 2-chains, $B_1(\mathcal{A}) = 0$. Hence, the homology of $\mathcal{A}$ is given by:

$$H_1(\mathcal{A}) = \frac{Z_1(\mathcal{A})}{B_1(\mathcal{A})} \cong \frac{\mathbb{Z}^2}{0} = \mathbb{Z}^2 \tag{4.3}$$

This is the result one would expect for homotopy: there exists a set of nontrivial homotopy classes for each independent cycle, since each independent cycle corresponds to a hole. However, the process has now been reduced to one of simple linear algebra.

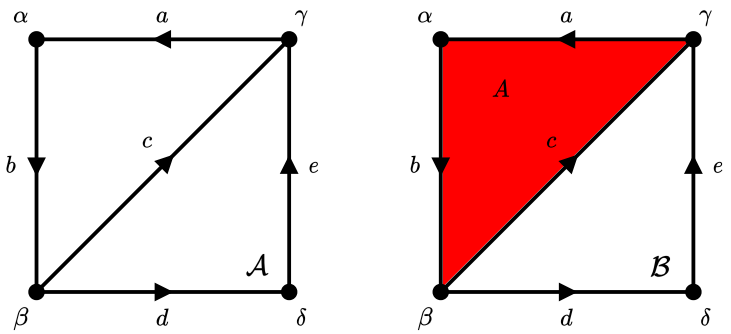

Figure 4.2: Two graphs $\mathcal{A}$ and $\mathcal{B}$. 0-cells (points) and 1-cells (lines) are labelled by greek and roman letters respectively. $\mathcal{B}$ differs from $\mathcal{A}$ by the presence of an additional 2-cell, labelled A, which fills one of the cycles.

Now let us consider $\mathcal{B}$. Since $\mathcal{A}$ and $\mathcal{B}$ are equivalent in terms of 0-chains and 1-chains, $Z_1(\mathcal{A}) = Z_1(\mathcal{B})$. However, $\mathcal{B}$ possesses an additional 2-chain given by A. Hence, $B_1(\mathcal{B})$ is no longer zero. Instead, since $\partial_2(A) = a+b+c$, it follows that $B_1(\mathcal{B}) = \text{im}\partial_2 = \langle a+b+c \rangle \cong \mathbb{Z}$. Hence, the homology of $\mathcal{B}$ is given by:

$$H_1(\mathcal{B}) = \frac{Z_1(\mathcal{B})}{B_1(\mathcal{B})} \cong \frac{\mathbb{Z}^2}{\mathbb{Z}} = \mathbb{Z} \tag{4.4}$$

Once again, this is precisely the expected result for homotopy. Namely, only one of the independent cycles contributes a set of nontrivial winding classes, since the other is filled by a 2-cell. This is the motivation behind computing cycles mod boundaries. Any independent cycle is a hole and hence contributes a set of nontrivial winding classes, unless it is filled by a higher dimensional cell.

To generalize this method to any smooth manifold, one can apply a preliminary *triangulation* step, in which the the manifold is first transformed into a simplicial complex using a homeomorphism (see Section 4.1.3). This general procedure of applying a homology computation following a triangulation is referred to as *simplicial homology*.

4.1.3 Simplices

A simplex is a higher dimension generalization of a triangle. If $\{\boldsymbol{v}_0, ..., \boldsymbol{v}_n\}$ is a set of $n+1$ points or vertices, then an n-simplex Δ_n is described by the convex hull of these points: $\sum_i c_i \boldsymbol{v}_i$ where $\sum_i c_i = 1$ and $0 \leq c_i \leq 1$ are the *barycentric coordinates*. Following this

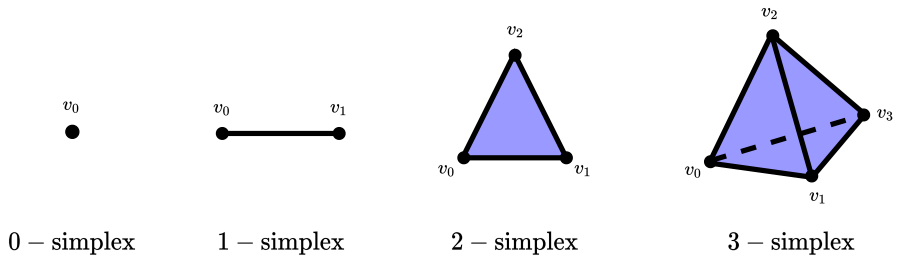

Figure 4.3: Illustration of first four simplices. The faces of any n-simplex are $n-1$ simplices. Both the 2-simplex and the 3-simplex are completely filled.

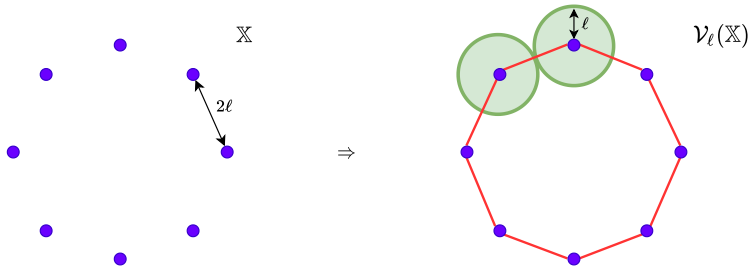

Figure 4.4: Point cloud $\mathbb{X}$ and associated VR complex $\mathcal{V}_\ell(\mathbb{X})$. At a radius of $r = \ell$, connections (1-simplices) form between all neighbouring points. The resulting complex is homeomorphic to a circle, and ultimately has a first Betti number of $b_1 = 1$.

definition, a 0-simplex is a point, a 1-simplex is a line, a 2-simplex is a filled triangle, and a 3-simplex is a filled tetrahedron (see Figure 4.3). It additionally follows that the faces of any n-simplex are $(n-1)$-simplices. More concretely, the boundary of any n-simplex is given by:

$$\partial(\Delta_n) = \sum_{\alpha=0}^{n} (-1)^\alpha \, (v_0 \cdots \hat{v}_i \cdots v_n) \tag{4.5}$$

where the hat symbol denotes omit and each term in the sum denotes an oriented face of the simplex. Following this definition, a *simplicial complex* is simply a set of connected and disconnected simplices satisfying the following rule: any two simplices that intersect must share a common face.

4.1.4 Vietoris-Rips Complex

The Vietoris-Rips (VR) complex is a tool for extending homology to point clouds [25]. As an example, we consider the set of points $\mathbb{X}$ shown in Figure 4.4. As a set of points, $\mathbb{X}$ has no topology ($b_n = 0\ \forall n$). However, it is clear that $\mathbb{X}$ has an underlying loop structure. To identify this loop structure, one can consider the ℓ VR complex of $\mathbb{X}$, denoted $\mathcal{V}_\ell(\mathbb{X})$. In this simple case, the $\mathcal{V}_\ell(\mathbb{X})$ is constructed by forming connections (1-simplices or lines) between neighbouring points (all points within a distance of 2ℓ away from each other). The resulting graph, which is homeomorphic to a circle, clearly has a nontrivial first homology group given by $H_1(\mathcal{V}_\ell(\mathbb{X})) \cong \mathbb{Z}$. Ultimately, the VR complex construction has allowed us to assign a topology to $\mathbb{X}$, and the underlying loop structure has been successfully identified.

Generally, the r VR complex $\mathcal{V}_r(\mathbb{X})$ of a point cloud $\mathbb{X}$ is constructed by forming an n-simplex for every subset of $n+1$ data points, denoted $\{x_0, ..., x_n\} \subset \mathbb{X}$, satisfying $d(x_i, x_j) \leq 2r$, where d is the selected metric. For a D dimensional point cloud, this can be visualized as expanding D-spheres of radius r around each point. If the spheres of two points overlap, a 1-simplex (line) is formed using these points. If the spheres of three points all overlap with each other, the a 2-simplex (filled triangle) is formed using these points. Generally, the formation of higher simplices is important for identifying higher homologies. For example, the nontrivial second homology associated with a 2-sphere can only be successfully identified under the formation of 2-simplices.

4.2 The Persistent Homology Algorithm

At this point, several questions arise. How does one know what radius to choose? And how does one measure the significance of these loop features? In regards to the latter question, one can imagine a scenario in which tinier loop structures exist on the edges of the circle considered in Figure 4.4. We consider such loop structures, which could be formed for example due to noise in a dataset, as being of less interest. To address these questions, one can compute the VR complexes $\mathcal{V}_r(\mathbb{X})$ and the resulting homology groups $H_n(\mathcal{V}_r(\mathbb{X}))$ for many different values of the radius r. The resulting sequence of VR complexes, with each element in the sequence corresponding to the formation of new simplices, is referred to as the *filtration* [25]. If a given loop structure forms at a radius r_b in the filtration and dies at a radius r_d in the filtration, then the significance (persistence) is measured by the difference in these radii: $p = r_d - r_b$.

To illustrate this procedure, we consider the example shown in Figure 4.5. As connections form and simplices are filled in, holes in the corresponding graph form and disappear.

In this particular example, two holes, labelled A and B, form at a radius of $2r = \ell$, where ℓ is the minimal distance between points. Holes A and B then disappear at a radius of $2r = \ell\sqrt{2}$ and $r = \ell$, due to the filling of simplices. Generally, the radius at which a hole forms and disappears is referred to as the *birth* and *death* of that hole, respectively. The significance of the corresponding loop structure in the data can then be measured as death minus birth, which is referred to as the *persistence* of the hole. In this case, the persistence of holes A and B are $p_A = 2\ell - \ell = \ell$ and $p_B = \ell\sqrt{2} - \ell \approx 0.4\ell$, respectively. Hence, A is regarded as a more significant topological feature in the data, since $p_A > p_B$. Persistence can be understood in terms of stability [46]: topological features with greater persistence are more stable against perturbations in the data. Ultimately, this procedure allows one to detect and measure the significance of all loop structures in the data, and is referred to as *persistent homology*.

4.3 Homology for the $\mathbb{Z}_2$ Gauge Theory

As discussed in Chapter 2, the ground state wavefunction of a general spin-1/2 string liquid can be understood as a quantum superposition over all closed string configurations. This holds if strings are formed over links of the direct lattice for which $\sigma^x = -1$, and similarly over links of the dual lattice for which $\sigma^z = -1$. Alternatively, these closed strings can be defined using the VR complex. If $\boldsymbol{\sigma}$ represents a configuration of spins, then we begin by defining $X_{\boldsymbol{\sigma}}$ as a graph consisting of a 0-simplex (point) at the location of each down spin. Closed strings can then be identified as nontrivial H_1 homologies of the corresponding VR complex at $r = \ell$: $\mathcal{V}_\ell(X_{\boldsymbol{\sigma}})$ where 2ℓ is the lattice spacing. Ultimately, each closed string will contribute to the first Betti number:

$$b_1(\boldsymbol{\sigma}) := \text{rank}(H_1(\mathcal{V}_\ell(X_{\boldsymbol{\sigma}}))), \tag{4.6}$$

while the size of each closed string can be measured by the persistence. Namely, in the persistent homology computation of $X_{\boldsymbol{\sigma}}$, each closed string will correspond to an H_1 birth-death point with $r_b = \ell$, while the size of each closed string can be measured as $r_d - r_b$. We note that b_1 accounts for all closed strings except those of minimal size (those generated by applying a single gauge transformation to an initial configuration consisting of all up spins). Such loops correspond to H_1 birth-death points with $r_b = \ell/\sqrt{2}$ and $r_d = \ell$. Examples of closed strings are shown in Figure 4.6 for the case of a $D = 2$ square lattice.

What about ground state configurations of the classical $\mathbb{Z}_2$ gauge theory in $D = 3$? In Figure 4.7, we show the VR complexes of graphs $X_{\boldsymbol{\sigma}'}$ and $X_{\boldsymbol{\sigma}''}$, where $\boldsymbol{\sigma}'$ ($\boldsymbol{\sigma}''$) are generated by applying one (two) gauge transformations to an initial configuration consisting solely

of up spins. The complex shown in Figure 4.7a for $\boldsymbol{\sigma}'$ holds generally for $\ell/\sqrt{2} \leq r < \ell$. Such a complex, which is homeomorphic to a hollow sphere, possesses second Betti number $b_2 = 1$.

The complex shown in Figure 4.7b for $\boldsymbol{\sigma}''$ holds generally for $\ell \leq r < \ell\sqrt{3/2}$. Such a complex is homeomorphic to a sphere with 4 holes. This in turn is homeomorphic to a plane with 3 holes: simply imagine expanding one hole. Hence, the corresponding first Betti number is $b_1 = 3$.

Applying a string of adjacent gauge transformations can then be understood as "gluing" planes with holes. Generally, if $\boldsymbol{\sigma}^n$ is generated by applying n adjacent gauge transformations to a configuration consisting of all up spins, then the number of holes is given by $b_1(\boldsymbol{\sigma}^n) = 3n$. On the other hand, generating vison defects through spin flips can be understood as eliminating connections (1-simplices) in the complexes considered above. Hence, vison defects will generally reduce the number of holes, and one expects $\langle b_1 \rangle$ to decrease with increasing T.

4.4 Numerical Results

To generate configuration data for the classical $\mathbb{Z}_2$ gauge theory in arbitrary dimensions, we employ a standard classical Monte Carlo method, consisting of cluster updates ($\mathbb{Z}_2$ gauge transformations) and local updates (spin flips) to sample the state at finite temperature according to the Metropolis algorithm. Then, persistent homology calculations are done on this configurational data using the Python Ripser package [2]. To reduce computational runtime, we set the *threshold* parameter (the radius r at which to stop the persistent homology computation) to 2 for the $3D$ case. It is additionally possible to restrict the computation to lower homology groups. Furthermore, to account for the periodic boundary conditions, we use the following modified metric:

$$d(\boldsymbol{x}, \boldsymbol{y}) = \sqrt{\sum_{\alpha=1}^{D} \min\left[y_\alpha - x_\alpha, (x_\alpha - \ell_1) + (\ell_2 - y_\alpha)\right]^2} \tag{4.7}$$

where $y_\alpha > x_\alpha$ and $\ell_2 > \ell_1$ are the locations of the boundaries. In our case, $\ell_1 = 0$ and $\ell_2 = L$, and any data point $\boldsymbol{x}$ will correspond to the location of a down spin on the lattice.

Generally, the n^{th} Betti number b_n of the $\mathcal{V}_r$ complex of a Monte Carlo configuration $\boldsymbol{\sigma}$ will be given by the number of H_n birth-death points in the persistent homology computation with birth value $r_b \leq r$ and $r_d > r$. In the remaining sections, we will compute the

expectation value of $\langle b_1 \rangle$ averaged over an ensemble of Monte Carlo sampled configurations for various temperatures T.

4.4.1 Two dimensional $\mathbb{Z}_2$ gauge theory

We begin by examining the $D = 2$ case. In Figure 4.8, average loop densities $\langle b_1 \rangle / L^2$ are shown for various temperatures and lattice sizes $N = 2 \times L \times L$, with 2000 Monte Carlo samples used for each temperature. We find that the frequency of closed strings generally decreases with increasing T. This is expected: as the temperature increases, vison defects (open strings) generate and hence reduce the number of closed strings.

Figure 4.8 additionally reveals that smaller system sizes possess slightly larger loop densities. In other words, we find that $\langle b_1 \rangle$ is not perfectly extensive. Recalling Figure 4.6, the size of a closed loop can be measured by the corresponding persistence value, which is given by $p = r_d - r_b$. In Table 4.1, we show the total frequency of loops with various death values and birth value $r_b = \ell$. Here, we observe that the the frequency of loops with death value $r_d = 3\ell$ is larger for $L = 8$, despite being the smallest system size. On the other hand, loops with death values $r_d > 3\ell$ occur for all sizes but $L = 8$. This is consistent with the deviation of $\langle b_1 \rangle$ from perfect extensiveness. While their are no dynamics in a loop condensate, it would make sense that the frequency of loops of larger sizes is restricted by the size of the lattice. If larger loops are more likely to form for larger system sizes, then one would expect the average loop density to decrease. Such an argument is weaker when comparing two larger system sizes, since there is an overall limit to the size of loops that can form.

This data confirms the general expectation that $\langle b_1(T) \rangle$ decreases with increasing temperature. However, since the $2D$ gauge theory has no phase transition at any non-zero temperature, the data in Figure 4.8 shows no sharp features or non-analytic behavior. One can ask the question whether this quantity behaves different in the presence of a phase transition. To this end, we next consider the $3D$ case, which has a critical point at $T_c \approx 1.314$. In other words, we ask under the VR complex construction, can the first Betti number be used to detect the deconfinement transition between the topologically ordered and disordered regimes?

4.4.2 Three dimensional $\mathbb{Z}_2$ gauge theory

To examine the $D = 3$ case, we use our Monte Carlo simulation of Equation 3.1 on a cubic lattice to produce 1000 samples at each temperature for various lattice sizes. Figure

r_d/ℓ	$\sqrt{2}$	$\sqrt{2.5}$	$\sqrt{4.5}$	3	$\sqrt{10}$	$\sqrt{12.5}$	$\sqrt{13}$
$L = 8$	124.73	151.30	57.47	59.55	0	0	0
$L = 16$	125.65	150.90	59.99	1.28	35	9	1
$L = 24$	125.63	149.28	60.16	2.20	164	59	3
$L = 32$	124.59	149.45	60.14	3.06	562	188	12

Table 4.1: Frequencies of H_1 birth-death points with birth value $r_b = \ell$ and various death values r_d. Based on 2000 Monte Carlo samples used to generate Figure 4.8 with $T = 0.02$. No vison defects are present. Frequencies for $2 \leq r_d \leq 3$ are divided by L^2 and rounded to 2 decimal places to illustrate minimal changes in density.

	$r_b = \ell$			$r_b = \ell/\sqrt{2}$			
r_d/ℓ	$\sqrt{3/2}$	$\sqrt{2}$	$\sqrt{5/2}$	$\sqrt{3/2}$	$\sqrt{2}$	2	> 2
$L = 6$	774.52	8.76	0.05	97.65	7.09	13.88	0
$L = 10$	779.81	8.93	0.10	99.25	10.06	0	3.00
$L = 14$	778.77	8.85	0.09	98.73	11.27	0	1.09
$L = 18$	778.82	8.87	0.09	98.81	11.72	0	0.51

Table 4.2: Frequencies of H_1 birth-death points over 1000 Monte Carlo samples (divided by L^3). Based on 1000 Monte Carlo samples used to generate Figure 4.10 with $T = 0.7$. No vison defects are present. Frequencies are divided by L^3 and rounded to 2 decimal places.

4.9 shows the value of $\langle b_1 \rangle$ for various linear system sizes L as a function of temperature. Similar to the $D = 2$ case, we find that the first Betti number increases with decreasing temperature, as expected in the case of decreasing vison defects, and that smaller system sizes have slightly larger loop densities. Once again, we see that from Table 4.2 that is due to the presence of larger loops in larger system sizes. Namely, loops with birth value $r_b = \ell/\sqrt{2}$ and death value $r_d = 2\ell$ occur only in $L = 6$, while loops with the same birth value and larger death values only occur in the larger system sizes. Among these larger system sizes, we see that the frequencies of loops with $r_d > 2\ell$ decreases with increasing system size, which again agrees with the idea that larger loops are more prominent in larger system sizes, hence reducing the overall frequency of loops.

The temperature range in Figure 4.9 includes the known value of the critical temperature in the $3D$ model, at $T_c \approx 1.314$. It is clear from the data that $\langle b_1 \rangle$ has a sharp feature at T_c, indicating that this quantity is sensitive to critical fluctuations that are manifest in the loop structures present in the spin configurations. Above the critical temperature, we

see a particularly rapid rise in $\langle b_1 \rangle$ as the transition is approached. We find that this can be accurately fit to $\langle b_1(T) \rangle \sim (T - T_c)^{\phi}$, where $\phi \approx 0.544$ is an estimate obtained from the largest system size considered in Figure 4.9.

Finally, we note that the full Betti number (all loops with birth values $r_b \leq \ell$ and death values $r_d > \ell$) is not required to detect this transition. As an example, Figure 4.10 shows the frequency of loops with birth value $r_b = \ell$ and death value $r_d = \ell\sqrt{3/2}$. As before, we find that the deconfinement transition is detected by a sharp feature in the average frequency. Note the exact structure of these loops was discussed in Section 4.3. Once again, if we assume that the expectation value takes the form $(T - T_c)^{\phi}$ for $T > T_c$, then we can obtain a value of $\phi \approx 0.582$ from the largest system size considered.

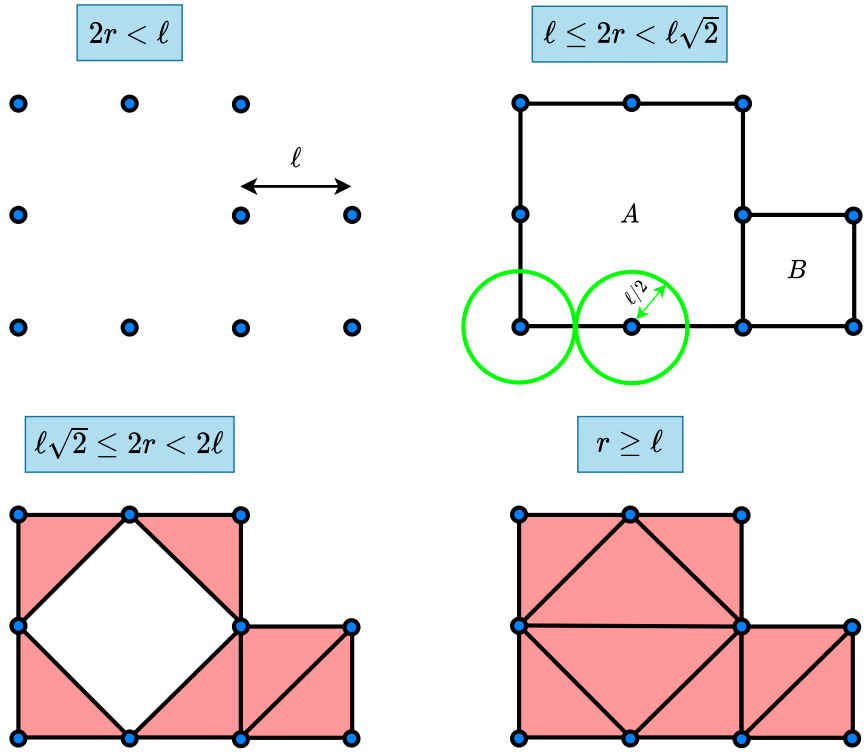

Figure 4.5: Illustration of persistent homology applied to a set of data points (blue dots). For any radius $2r < \ell$, no circles overlap, and hence, no connections form. At a radius of $2r = \ell$, all points within a distance of ℓ from each other form connections. The corresponding graph has 2 holes, labelled A and B. Since these holes form exactly at $2r = \ell$, they are said to be *born* at $2r = \ell$. At a radius of $2r = \ell\sqrt{2}$, diagonal connections of length $\ell\sqrt{2}$ form, and the resulting simplices (triangles) are filled in (pink). Since hole B is no longer present, it is said to have *died* at $2r = \ell\sqrt{2}$. Similarly, at a radius of $r = \ell$, one final connection forms, and two more simplices are filled in. Since hole A is no longer present, it is said to have *died* at $r = \ell$. To measure the significance of each hole, one can compute the *persistence* as death minus birth. These are given by $p_A = 2\ell - \ell = \ell$ and $p_B = \ell\sqrt{2} - \ell \approx 0.4\ell$ for holes A and B, respectively. Since hole A has a greater persistence than hole B, it is considered to be a more significant topological feature in the data.

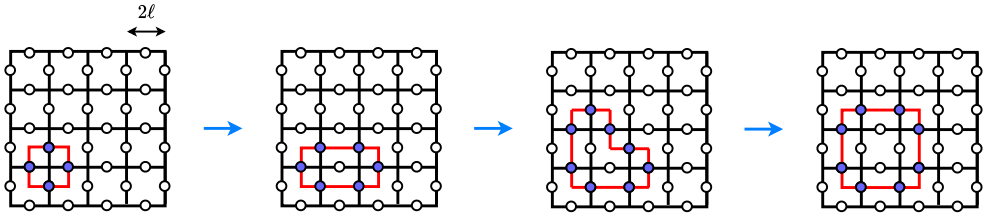

Figure 4.6: Examples of $\mathcal{V}_\ell$ complex constructions of ground state configurations of the $\mathbb{Z}_2$ gauge theory, where blue dots depict down spins. The first configuration is generated by the application of a single gauge transformation to a configuration consisting solely of up spins, which generates a closed string of minimal size. Such a configuration corresponds to an H_1 homology that is born at $r = \ell/\sqrt{2}$ and dies at $r = \ell$. Arrows depict steps in which single adjacent gauge transformations are applied, which stretches this loop to greater sizes. In the context of persistent homology, this corresponds to generating loops of greater persistence. The remaining three configurations correspond to H_1 homologies that are born at $r = \ell$ and die at $r = \left\{\ell\sqrt{2}, \ell\sqrt{5/2}, \ell\sqrt{9/2}\right\}$ respectively.

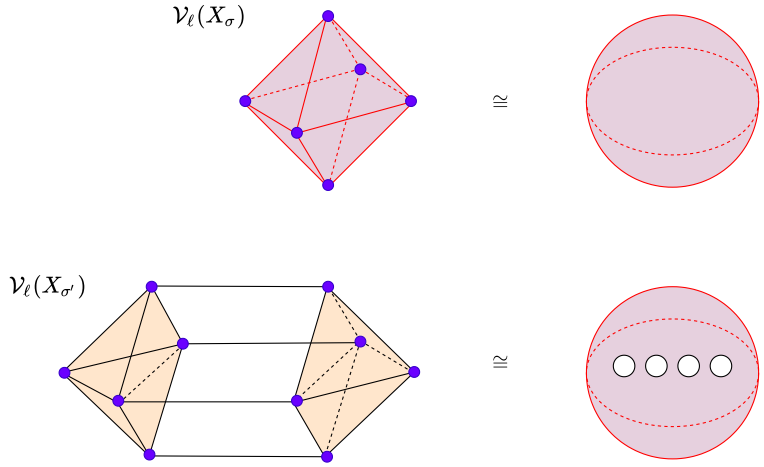

Figure 4.7: Top (bottom): Illustration of VR complex corresponding to $\boldsymbol{\sigma}'$ ($\boldsymbol{\sigma}''$), which is generated by applying one (two) gauge transformations to a configuration consisting solely of up spins. Blue points depict down spins. Red structures are hollow and beige structures are filled. The top VR complex of $\boldsymbol{\sigma}'$ holds generally for $\ell/\sqrt{2} \leq r < \ell$. The bottom VR complex of $\boldsymbol{\sigma}''$ holds generally for $\ell \leq r < \ell\sqrt{3/2}$. $\cong$ denotes homotopic equivalence.

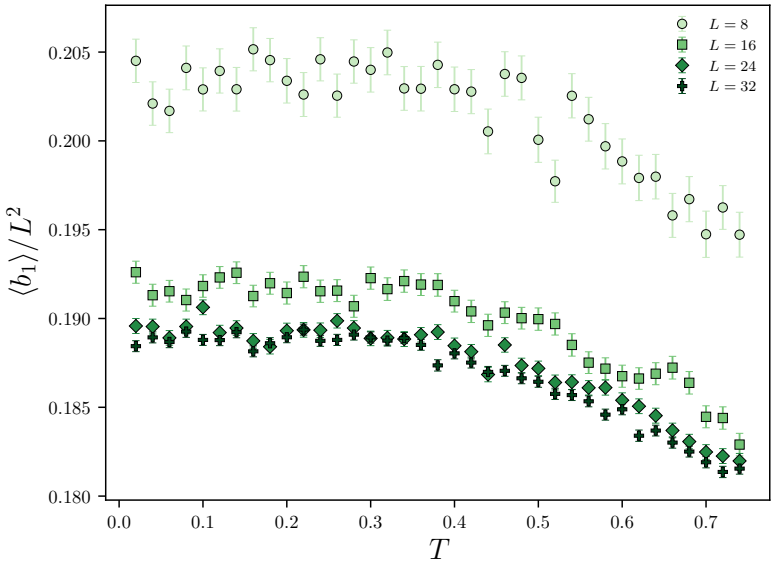

Figure 4.8: Average first Betti number of $r = \ell$ VR complexes of configurations in the $\mathbb{Z}_2$ gauge theory with $D = 2$. $\langle b_1 \rangle$ is averaged over 2000 samples for each temperature. Standard errors bars defined as 99% Gaussian confidence intervals.

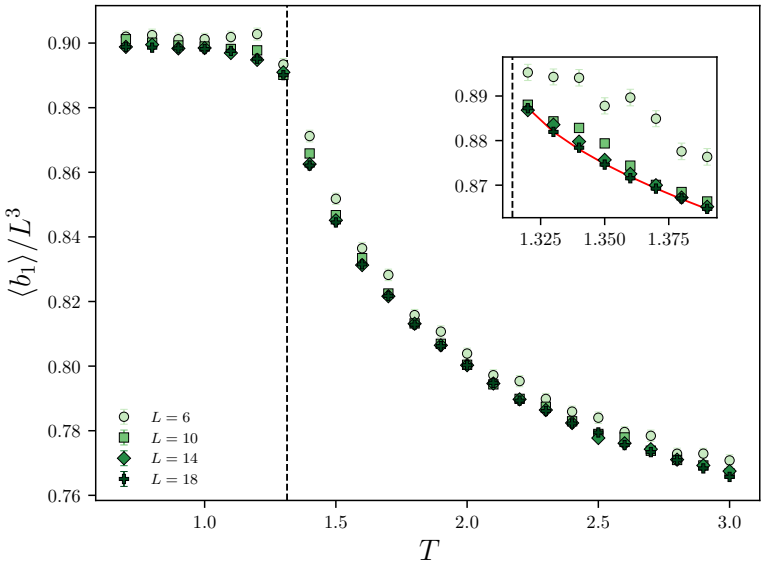

Figure 4.9: Average first Betti number of $r = \ell$ VR complexes of configurations in the $\mathbb{Z}_2$ gauge theory with $D = 3$. $\langle b_1 \rangle$ is averaged over 1000 samples for each temperature. Dashed line indicates theoretical value of critical temperature. Location of the phase transition is correctly identified by a change in the concavity of $\langle b_1 \rangle$. Statistical error bars are not visible.

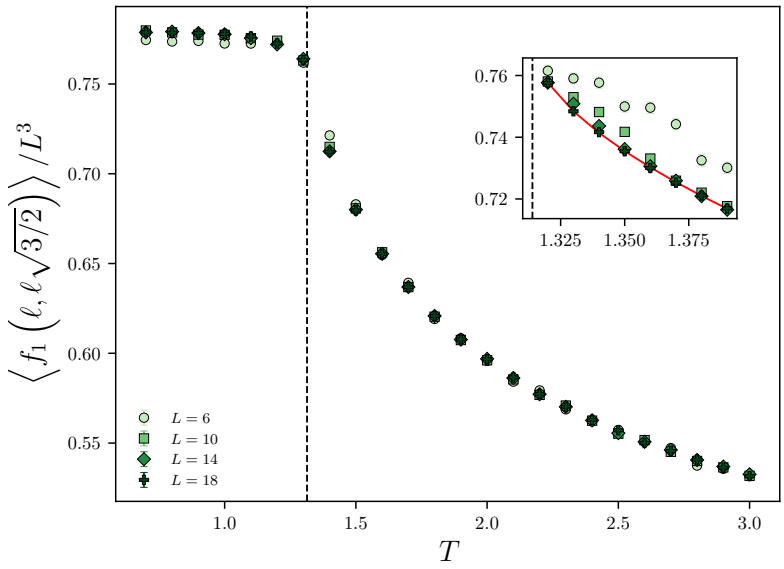

Figure 4.10: Average frequency of H_1 homologies with birth and death values $r_b = \ell$ and $r_d = \ell\sqrt{3/2}$. Based on the same Monte Carlo configurations used in Figure 4.9.

Chapter 5

$\mathbb{Z}_4$ Topological Order in Weyl Semimetals

In the previous chapters, we discussed topological order in the context of lattice spin systems. Topological order can also occur in electron fluids, and the most well-known example of this is the 2D fractional quantum Hall (FQH) liquid. This chapter will be structured as follows. First, we will provide a brief review of topological order in the context of the 2D FQH liquid. Next, we will review band topology and Weyl semimetals, which are defined by the separation of Weyl fermions of opposite chirality in momentum space, and possess a chiral anomaly response. Finally, we will review an alternative construction of an electron system with topological order using a Weyl semimetal, which involves gapping a Weyl semimetal with superconducting pairing and condensing flux 4π superconducting vortices [33, 34]. We will show that this $\mathbb{Z}_4$ topological order can alternatively be constructed from charge density wave interactions, and will derive the surface state Lagrangian for the BF theory of this topological order.

5.1 2D Fractional Quantum Hall Liquids

5.1.1 Integer Quantum Hall Effect

The physical setup for the classical Hall effect simply consists of a current travelling through a 2D slab, and a magnetic field that is perpendicular to the slab. Such a magnetic field induces a Lorentz force on the electrons, which causes the accumulation of electrons at one

end of the slab. At a certain point, this polarization of charge induces an electric force that is equal and opposite to the Lorentz force, which prevents further accumulation of charge. The resulting potential difference across the slab is called the *Hall voltage* V_H. The quantum Hall effect refers to cases where the resulting Hall conductance is quantized in units of e^2/h:

$$\sigma = \frac{I}{V_H} = \nu \frac{e^2}{h}$$

where $\nu \in \mathbb{Z}$. In a 2D electron gas with a uniform magnetic field B, the energy levels are given by $E_n = \hbar\omega_c(n + 1/2)$ where $\omega_c = eB/mc$ and are referred to as *Landau levels*. The total number of states that can be occupied by each Landau level are given by $N_\phi = \phi/\phi_0$ where $\phi := L_x L_y B$ is the total magnetic flux through the sample and $\phi := hc/e$ is the magnetic flux quantum. Hence, increasing the external magnetic field B or the area of the slab $A = L_x L_y$ increases the number of allowed states per Landau level. Ultimately, one can show that ν directly corresponds to the number of filled Landau levels, and hence is referred to as the *Landau filling factor* [36].

5.1.2 Fractional Quantum Hall Effect

It turns out that it is possible to obtain fractional filling of the Landau levels for certain values of the external magnetic field. Such phases generally possess topological order. In the case of Laughlin states, which refer to states with filling factor $\nu = 1/m$, quasi-hole and quasi-particle excitations can each be shown to have fractional exchange statistics $\theta = \pi/m$ and fractional charges $e^* = \pm e/m$ [36]. Topological degeneracy then becomes a direct consequence of these anyons. Following the argument of [36], one can define two cycle operators T_1 and T_2, which create a pair of quasi-hole and quasi-particle anyons, and move these anyons around of two topologically distinct non-contractible loops of the torus, before annihilating. It follows that $T_1 T_2 T_1^{-1} T_2^{-1}$ corresponds to taking one anyon around the other. For anyons with statistics $\theta = \pi/m$, it then follows that $T_1 T_2 = e^{2\pi i/m} T_2 T_1$. The smallest representation of this algebra has dimension m:

$$\begin{aligned} T_1 \left|n\right\rangle &= e^{2\pi n i/m} \left|n\right\rangle \\ T_2 \left|n\right\rangle &= \left|n+1\right\rangle \end{aligned}$$

and hence the topological ground state degeneracy is m. This generalizes to m^g on a Σ_g Riemann surface [47].

5.2 Topological Semimetals

As mentioned in the beginning of this chapter, our goal will be to discuss an alternative construction to topological order in electron systems involving Weyl semimetals. Hence, this section will be dedicated to reviewing the defining features and resulting responses of Weyl semimetals. To begin with, we will review topology in the context of band theory, where we follow along [36, 48].

5.2.1 Topological Band Theory

Let us consider the eigenstates $|n(\boldsymbol{\lambda})\rangle$ of a Hamiltonian $H(\boldsymbol{\lambda})$ parameterized by $\boldsymbol{\lambda}$. If the parameters $\boldsymbol{\lambda}$ are varied sufficiently slowly, a system that begins in eigenstate $|n(\boldsymbol{\lambda})\rangle$ will remain in that eigenstate, assuming that this eigenstate at no point becomes degenerate with any other eigenstate (i.e. there are no *level crossings*). This famous result is known as the *adiabatic theorem*. It follows then that if we begin in the n^{th} energy eigenstate and complete an adiabatic time evolution along a closed loop in parameter space, such that $\boldsymbol{\lambda}(t_0) = \boldsymbol{\lambda}(t_f)$ for initial and final times t_0 and t_f, then the final state will simply differ from the initial state by a phase. This phase includes the expected dynamical phase of the form $e^{-i\int dt E_n(t)/h}$ where $E_n(t)$ is the energy corresponding to the n^{th} eigenstate at a given time t. However, it includes an additional contribution known as the *Berry phase* [49]:

$$e^{i\gamma} = \exp\left(-i\oint_{\mathcal{C}} \mathcal{A}_i(\lambda) d\lambda^i\right) \tag{5.1}$$

where $\mathcal{C}$ defines the closed loop in parameter space and $\mathcal{A}_i(\lambda)$ is the *Berry connection*:

$$\mathcal{A}_i(\lambda) = -i\langle n|\,\partial_{\lambda_i}\,|n\rangle \tag{5.2}$$

Since the Berry phase has no time dependence and depends only on the geometry of the loop in parameter space, it is sometimes referred to as the *geometric phase*. In the context of the differential geometry of surfaces, γ can be interpreted as a *holonomy angle*, which is the angle by which a vector rotates upon parallel transport around the closed curve $\mathcal{C}$. Such a quantity will generally depend on the geometry of the surface being considered, and is computed as the line integral of the connection along $\mathcal{C}$. In our case, the surface is defined in the parameter space of the Hamiltonian, and the Berry phase is the holonomy angle of a state vector after parallel transport around a closed parameter curve representing physical adiabatic time evolution. One can also define the *Berry curvature*:

$$\mathcal{F}_{ij}(\lambda) = \frac{\partial \mathcal{A}_j}{\partial \lambda^i} - \frac{\partial \mathcal{A}_i}{\partial \lambda^j} \tag{5.3}$$

from which it follows by Stoke's theorem that:

$$e^{i\gamma} = \exp\left(-i \oint_{\mathcal{C}} \mathcal{A}_i(\lambda) d\lambda^i\right) = \exp\left(-i \iint_S \mathcal{F}_{ij} dS^{ij}\right) \tag{5.4}$$

where S is the region enclosed by $\mathcal{C}$. In the context of surfaces, the integral of the curl of the connection on an open surface S has the interpretation of the total curvature of S. If such an integral is computed over an entire manifold $\mathcal{M}$, then the value of this integral also has a direct relationship to the topology of $\mathcal{M}$:

$$\oiint_{\mathcal{M}} \mathcal{F}_{ij} dS^{ij} = 2\pi\chi(\mathcal{M}) = 4\pi(1-g) \tag{5.5}$$

where $\chi(\mathcal{M})$ is a topological invariant of $\mathcal{M}$ known as the *Euler's characteristic* and g is the number of holes or *genus* of $\mathcal{M}$. This remarkable theorem, which provides a direct relationship between local geometry and global topology, is known as the *Gauss-Bonnet* theorem. In our context, $\chi(\mathcal{M})$ is commonly denoted C and is referred to as the *Chern number* or *Chern invariant*. While a complete proof of the Gauss Bonnet theorem is complicated, it is easy to see that the integral of the curvature over any closed surface must be quantized in units of 2π. Notice that in transforming the line integral of the connection to a surface integral of the curvature, there is some freedom in regards to which surface to choose. Namely, one can choose either the interior or exterior region. Let us call the resulting Berry phases γ_1 and γ_2.

$$\gamma_1 = \iint_{\text{inner}} \mathcal{F}_{ij} dS^{ij} \tag{5.6}$$

$$\gamma_2 = \iint_{\text{outer}} \mathcal{F}_{ij} dS^{ij} \tag{5.7}$$

Consistency requires that $e^{i\gamma_1} = e^{i\gamma_2}$ and hence $\gamma_2 = \gamma_1 + 2\pi C$ where C is an integer. In the limit that the interior region is made infinitely small, we obtain:

$$\oiint_S \mathcal{F}_{ij} dS^{ij} = 2\pi C \tag{5.8}$$

Equation 5.8 is sometimes called the *Gauss-Bonnet-Chern* theorem. Interestingly, this equation reduces to the Dirac quantization condition for magnetic monopoles in the case

of a spin in a magnetic field. In the case of a particle of charge q moving along a closed-loop with enclosed magnetic flux ϕ, the resulting Berry phase is given by $e^{iq\phi}$ [36]. This is the *Aharonov-Bohm effect*.

Ultimately, we see that integration of the Berry curvature over a closed region in the parameter space of a Hamiltonian defines a topological invariant C. Namely, the Chern number C will remain unchanged as long as the topology of the surface defined by the Hamiltonian remains unchanged. As one could imagine, the robustness of a Chern invariant to local perturbations in the parameters of a Hamiltonian would be useful in the context of encoding fault-tolerant quantum information, which is indeed an active field of research [9]. As we will see, Weyl semimetals are one example of materials with non-trivial band topology.

5.2.2 Weyl Semimetals

Weyl fermions are described by the massless Dirac equation in odd spatial dimensions [50]. In three spatial dimensions, the massless Dirac equation simplifies to:

$$i\partial_t \psi_\pm = H_\pm \psi_\pm \tag{5.9}$$

where $H_\pm = \mp \boldsymbol{p} \cdot \boldsymbol{\sigma}$. This describes fermions that propagate parallel or anti-parallel to their spin, which defines their chirality. Generally, Weyl fermions must always exist in pairs of opposite chirality. However, Weyl fermions of opposite chirality can be separated in momentum space. Such materials possessing this momentum-space separation of Weyl fermions are referred to as *Weyl semimetals*. To make this concrete, we will review the example provided in [51], which considers the following Hamiltonian:

$$H = v_F \tau^z \boldsymbol{\sigma} \cdot \boldsymbol{k} + \Delta \tau^z \tag{5.10}$$

where $\boldsymbol{\tau}$ is an additional set of Pauli matrices that describes the two nodes. Equation 5.10 describes a single pair of opposite chirality Weyl nodes located at the same crystal momentum. One can separate these nodes by imposing an external magnetic field:

$$H = v_F \tau^z \boldsymbol{\sigma} \cdot \boldsymbol{k} + \Delta \tau^z + b\sigma^z \tag{5.11}$$

To see this, one can diagonalize the σ^z block of the Hamiltonian upon applying canonical transformations $\sigma^\pm \to \tau^z \sigma^\pm$ and $\tau^\pm \to \sigma^z \tau^\pm$. The Hamiltonian then reduces to:

$$H_\pm = v_F(\sigma^x k_x + \sigma^y k_y) + m_\pm(k_z)\sigma^z \tag{5.12}$$

Where $m_{\pm}(k_z) = b \pm \sqrt{v_F^2 k_z^2 + \Delta^2}$. We see that $m_-(k_z) = 0$ if $k_z = \pm k_0$ where $k_0 = \frac{1}{v_F}\sqrt{b^2 - \Delta^2}$. Since the Hamiltonian takes the form $H = \pm v_F \boldsymbol{\sigma} \cdot \boldsymbol{k}$ at these values of k_z, gapless nodes hosting Weyl fermions of opposite chirality are indeed present in these locations in momentum space. Such nodes are referred to as *Weyl nodes*. In the vicinity of a Weyl node, the Berry curvature takes a universal form $\boldsymbol{F}(\boldsymbol{k}) = \pm \boldsymbol{k}/2k^3$ such that

$$C = \frac{1}{2\pi} \int \boldsymbol{F}(\boldsymbol{k}) \cdot d\boldsymbol{S} = \pm 1 \tag{5.13}$$

where the sign refers to the chirality of the Weyl node. Namely, Weyl nodes can be be viewed as point sources or sinks of Berry curvature, and hence are topologically protected! The non-zero Chern number associated with a Weyl node at a given point in momentum space is sometimes referred to as the *topological charge* of that point [52].

5.2.3 Chiral Anomaly

The fact that Weyl nodes are topologically protected implies that any responses defined by the momentum space separation of Weyl fermions of opposite chirality are also topologically protected. One response resulting from the presence of Weyl nodes is the presence of chiral edge modes in the region of momentum space existing between the two Weyl nodes. For the concrete example shown above, [52] indeed shows that there exists chiral zero energy states localized at the boundary as long as $-k_0 \leq k_z < k_0$. Such an interval in momentum space is referred to as the *Fermi arc*, and the resulting surface states are referred to as *Fermi arc surface states*.

Several more interesting responses can be obtained upon the application of an external electromagnetic field. Generally, the pairing of Weyl fermions in momentum space can be understood as as direct consequence of the Nielsen-Ninomiya theorem, which states that Weyl fermions must generally exist in pairs of opposite chirality. It is however possible to break this conservation of chiral charge by imposing an external electromagnetic field. Namely, applying an electric field $\mathcal{E}$ over a time interval Δt will induce a momentum shift $\Delta p = e\mathcal{E}\Delta t$ for the charged particles. This is the *chiral anomaly* and is described as [52]:

$$\partial_\mu j_5^\mu = \frac{e^2}{2\pi^2} \boldsymbol{E} \cdot \boldsymbol{B} \tag{5.14}$$

To see that this anomaly has physically observable consequences, we begin by noting that this equation can be obtained from the following action for an electromagnetic field:

$$S = -\frac{e^2}{4\pi^2} \int dt d^3 r b_\mu \epsilon^{\mu\nu\alpha\beta} A_\nu \partial_\alpha A_\beta \tag{5.15}$$

where $b^\mu = (b_0, -\boldsymbol{b})$ couples to the chiral current j_5^μ just as the electromagnetic gauge field A_μ couples to the ordinary current j^μ. Hence, b^μ is referred to as the *chiral gauge field*. In the context of Weyl semimetals, one can show that b_0 and $\boldsymbol{b}$ describe the energy and momentum space separation of the Weyl nodes [52]. Topological responses can then be obtained upon varying the action with respect to the electromagnetic gauge field A_μ:

$$\boldsymbol{j} = \frac{e^2}{2\pi^2}(\boldsymbol{E} \times \boldsymbol{b}) \tag{5.16}$$

$$\boldsymbol{j} = \frac{e^2}{2\pi^2} b_0 \boldsymbol{B} \tag{5.17}$$

The first of the two equations describes an electrical conductance that is proportional to the momentum space space separation of the Weyl nodes: $\sigma_{xy} = \frac{e^2}{h}\frac{2|\boldsymbol{b}|}{2\pi}$. The second of the two equations describes a current along a magnetic field under the presence of energy space separation between the Weyl nodes. This is referred to as the *chiral magnetic effect* and is described in more detail in [52].

5.3 Topological Order in Weyl Semimetals

In Wang et al. [33], the question was asked as to whether or not it is possible to gap Weyl semimetals while preserving the electrical and thermal responses resulting from the chiral anomaly. To begin with, they consider gapping the Weyl nodes with superconducting pairing. The presence of such interactions breaks translational symmetry due to density modulations, and breaks charge conservation symmetry due to the formation of a Cooper pair condensate. They then show that it is indeed possible to restore these symmetries and ultimately the original chiral anomaly response by condensing flux 4π vortices in the superconducting order parameter at a Weyl node separation of $2Q = \pi$. In this case, the remaining uncondensed $\Phi = n\pi$ loops for $n < 4$ survive as gapped excitations with non-trivial statistics. Namely, they show that the intersection of an odd flux loop with an atomic xy plane induces a Majorana zero mode, which implies non-Abelian statistics of loop braiding. Furthermore, they show that the intersection of a $\Phi = 2\pi$ loop with an atomic xy plane induces a semion, which implies non-trivial Abelian statistics of loop braiding. Hence, the resulting state possesses $\mathbb{Z}_4$ topological order. In a follow-up paper by M. Thakurathi and A. Burkov [34], the hydrodynamic BF theory for this model was derived. Before proceeding to the work done in this thesis, we will review their derivation of the field theory for the model first proposed in [33].

5.3.1 The Hydrodynamic BF Theory

Ref. [34] begins by considering the following Hamiltonian for a gapless Weyl semimetal [53, 54]:

$$H = \sum_k \psi_k^\dagger \left[\sigma_x \sin(k_x) + \sigma_y \sin(k_y) + \sigma_z m(k)\right] \psi_k \tag{5.18}$$

where σ_i describes the pair of touching bands. This Hamiltonian describes Weyl nodes located at $k_z = \pm Q$. The charge and spin degrees of freedom of the electron operator ψ_r can be separated by first considering the following parton representation: $\psi_r = e^{i\theta_r} f_r$ where $e^{i\theta_r}$ represents a charged boson and f_r represents a neutral fermion [55]. If n_r is the chargon number operator, then we must have that $n_r = f_r^\dagger f_r$ and that $[\theta_r, n_r] = -i$. Decoupling of the spinon and chargon variables can then be accomplished by applying a Hubbard-Stratonovich transformation [56]. This gives $\mathcal{L} = \mathcal{L}_f(\chi, a_{r\mu}, f_r) + \mathcal{L}_b(\chi, a_{r\mu}, \theta_r)$ where χ and a_{ri} are the magnitude and phase of the Hubbard-Stratonovich field and a_{r0} is a Lagrange multiplier which enforces the constraint $n_r = f_r^\dagger f_r$ [57]. Upon the addition of Bardeen–Cooper–Schrieffer (BCS) pairing, the spinon Hamiltonian takes the form:

$$\begin{aligned} H &= \sum_k f_k^\dagger \left[\sigma_x \sin(k_x) + \sigma_y \sin(k_y) + m(k)\sigma_z\right] f_k + \Delta \sum_k \left(f_{k\uparrow}^\dagger f_{-k\downarrow}^\dagger + f_{-k\downarrow} f_{k\uparrow} \right) \\ &= \frac{1}{2} \sum_k \tilde{f}_k^\dagger \left\{\sigma_x \sin(k_x) + \sigma_y \sin(k_y) \; + [m(k) \pm \Delta]\sigma_z\right\} \tilde{f}_k \end{aligned}$$

where $\tilde{f}_k = \left(f_{k\uparrow}, f_{k\downarrow}, f_{-k\downarrow}^\dagger, f_{-k\uparrow}^\dagger\right)$ is the Nambu spinor. For $\Delta > 1$, this describes a gapped topological superconductor with a chiral Majorana edge mode and a zero-energy Majorana bound state in the $hc/2e = \pi$-flux vortex core [58, 59]. Vortex condensation can then be achieved upon considering the charge sector of the theory:

$$\mathcal{L}_b = i n_r \left(\partial_\tau \theta_r + A_{r0} + a_{r0}\right) - \chi \cos\left(\Delta_i \theta_r + A_{ri} + a_{ri}\right) \tag{5.19}$$

Decoupling the cosine term using a Villain transformation gives [60, 57]:

$$\mathcal{L}_b = i J_{r\mu} \left(\Delta_\mu \theta_r + A_{r\mu} + a_{r\mu}\right) + \frac{1}{2\chi} J_{r\mu}^2 \tag{5.20}$$

where $J_{r\mu}$ are integer chargon currents due to minimal coupling with the external electromagnetic gauge field $A_{r\mu}$, and exist on the links of the square lattice. Integrating out θ_r leads to a divergence-free constraint:

$$\Delta_\mu J_{r\mu} = 0 \tag{5.21}$$

which implies chargon conservation. This constraint can be solved as:

$$J_\mu = \frac{1}{4\pi}\epsilon_{\mu\nu\lambda\rho}\Delta_\nu b_{\lambda\rho} \tag{5.22}$$

where $b_{\mu\nu} \in 2\pi\mathbb{Z}$ are defined on plaquettes of the dual space-time lattice. This equation possesses gauge invariance with respect to the transformation: $b_{\mu\nu} \to b_{\mu\nu} + \Delta_\mu g_\nu - \Delta_\nu g_\mu$. Such a constraint on the two-form gauge field can be relaxed by introducing a cosine term:

$$\mathcal{L}_b = \frac{i}{2\pi}\left(A_\mu + a_\mu\right)\epsilon_{\mu\nu\lambda\rho}\Delta_\nu b_{\lambda\rho} + \frac{1}{8\pi^2\chi}\left(\epsilon_{\mu\nu\lambda\rho}\Delta_\nu b_{\lambda\rho}\right)^2 - t\cos\left(\Delta_\mu\alpha_\nu - \Delta_\nu\alpha_\mu + b_{\mu\nu}\right) \tag{5.23}$$

where α_μ satisfies the transformation law $\alpha_\mu \to \alpha_\mu - g_\mu$ under the gauge transformation $b_{\mu\nu} \to b_{\mu\nu} + \Delta_\mu g_\nu - \Delta_\nu g_\mu$ in order to ensure gauge invariance. Since $e^{-i\alpha_{r\mu}}$ is the creation operator for a vortex loop on the link (r,μ) of the dual lattice, the cosine term is a vortex kinetic energy term [61]. Conventional vortex condensation correspond to $t \gg 1$. This however results in a Meissner term for the gauge field $b_{\mu\nu}$ and produces a trivial Mott insulator with zero electrical Hall conductivity, which would correspond to the condensation of flux 2π vortices. This can be resolved by again decoupling the resulting cosine term using a Villain transformation:

$$\mathcal{L}_b = \frac{i}{2\pi}\left(A_\mu + a_\mu\right)\epsilon_{\mu\nu\lambda\rho}\Delta_\nu b_{\lambda\rho} + \frac{1}{8\pi^2\chi}\left(\epsilon_{\mu\nu\lambda\rho}\Delta_\nu b_{\lambda\rho}\right)^2 \tag{5.24}$$

$$+ iJ_{\mu\nu}\left(\Delta_\mu\alpha_\nu - \Delta_\nu\alpha_\mu + b_{\mu\nu}\right) + \frac{1}{2t}\left(J_{\mu\nu}\right)^2 \tag{5.25}$$

where $J_{\mu\nu}$ are integer vortex currents. Namely, $\Delta_\mu J_{\mu\nu} = 0$ follows from integrating out α_μ, which is a vorticity conservation law. This can be solved as

$$J_{\mu\nu} = \frac{1}{2\pi}\epsilon_{\mu\nu\lambda\rho}\Delta_\lambda c_\rho, \tag{5.26}$$

where $c_\mu \in 2\pi\mathbb{Z}$ are defined on the links of the original space-time lattice. This equation possesses gauge invariance with respect to the transformation: $c_\mu \to c_\mu + \partial_\mu f$. Integrating over c_μ produces a trivial Mott insulator. However, repeating the same procedure with a modified vortex kinetic energy term of the form $-t\cos\left(\Delta_\mu \alpha_\nu - \Delta_\nu \alpha_\mu + 2b_{\mu\nu}\right)$ produces responses consistent with the flux 4π vortex condensation considered in [33]. Namely, the resulting theory for the charge sector with the addition of a Chern-Simons term gives:

$$\mathcal{L}_b = \frac{i}{2\pi}\left(A_\mu + a_\mu + 2c_\mu\right)\epsilon_{\mu\nu\lambda\rho}\partial_\nu b_{\lambda\rho} - \frac{2i}{4\pi}\epsilon_{z\mu\nu\lambda}c_\mu\partial_\nu c_\lambda \tag{5.27}$$

Integrating out $b_{\mu\nu}$ gives $c_\mu = -\frac{A_\mu + a_\mu}{2}$. One can then justify the interpretation of $J_{\mu\nu}$ as a vortex current as follows. First, we note that Equation 5.20 simplifies to $\mathcal{L}_b = \left(\Delta_\mu \theta_r - 2c_\mu\right)^2$ upon varying with respect to J_μ. Minimizing the action then requires that $\nabla\theta = 2\boldsymbol{c}$. Then it follows that:

$$\oint \nabla\theta \cdot d\ell = 2\pi n = 2\oint c \cdot d\ell = 2\iint \nabla \times \boldsymbol{c} \cdot \boldsymbol{dS} = 4\pi \iint \boldsymbol{J_0} \cdot \boldsymbol{dS} \tag{5.28}$$

where the final equality follows from the fact that J_{0i} describes the magnetic field for c_μ:

$$J_{0i} = \frac{1}{2\pi}\epsilon_{ijk}\partial_j c_k = \frac{1}{2\pi}b_i \tag{5.29}$$

From the term $J_{0i}\partial_\tau \alpha_i$ in Equation 5.25 it follows that $[\alpha_i, J_{0i}] = i$ and hence that $e^{i\alpha_i}$ generates a vortex along direction i. The fact that $t \gg 1$ generates a trivial Mott insulator before taking $b_{\mu\nu} \to 2b_{\mu\nu}$ in the vortex kinetic energy term implies that $e^{i\alpha_i}$ specifically generates flux 2π vortices. This also follows from the observation that minimal coupling of $J_{\mu\nu}$ to the two-form gauge field $b_{\mu\nu}$ reveals that $J_{\mu\nu}$ describes charge-1/2 semions. Namely, one can consider minimally coupling the gauge fields $b_{\mu\nu}$ and c_μ to currents $j_{\mu\nu}$ and j_μ. With spinon coupling ignored, this gives:

$$\mathcal{L}_b = \frac{i}{2\pi}\left(A_\mu + 2c_\mu\right)\epsilon_{\mu\nu\lambda\rho}\partial_\nu b_{\lambda\rho} - \frac{2i}{4\pi}\epsilon_{z\mu\nu\lambda}c_\mu\partial_\nu c_\lambda + ib_{\mu\nu}j_{\mu\nu} + ic_\mu j_\mu \tag{5.30}$$

Setting $j_{\mu\nu} = 0$ and integrating out $b_{\mu\nu}$ gives:

$$\mathcal{L}_b = -\frac{i}{8\pi}\epsilon_{z\mu\nu\lambda}A_\mu\partial_\nu A_\lambda - \frac{i}{2}j_\mu A_\mu \tag{5.31}$$

which reveals that j_μ describes charge-1/2 bosons. The first term gives the expected electrical Hall conductivity $\sigma_{xy} = 1/4\pi$. For example, varying with respect to A_x gives:

$$j_x = \frac{i}{4\pi}(i\partial_t A_y + i\partial_y \varphi) = -\frac{1}{4\pi}(\partial_y \varphi + \partial_t A_y) = \frac{1}{4\pi} E_y$$

With the mean-field assumption that all fields are uniform in the z direction, setting $j_\mu = 0$ and integrating out c_μ gives:

$$\mathcal{L}_b = \frac{2i}{4\pi}\epsilon_{z\mu\nu\lambda} b_{\mu z}\partial_\nu b_{\lambda z} - \frac{i}{2\pi} A_\mu \epsilon_{z\mu\nu\lambda}\partial_\nu b_{\lambda z} + i b_{\mu z} j_{\mu z} \tag{5.32}$$

The Chern-Simons term for $b_{\mu z}$ implies that $j_{\mu z}$ describes particles with statistics $\theta = \pi/2$. This follows from the flux attachment argument. Namely, ignoring A_μ and varying with respect to $b_{\mu z}$ gives:

$$j_{\mu z} = \frac{1}{\pi}\epsilon_{\mu\nu\lambda}\partial_\nu b_{\lambda z}$$

which implies that a charged particle carries flux $\Phi = \pi$. Then it follows that the braiding of one such particle around the other induces a Aharonov-Bohm phase of $e^{i\Phi} = e^{i\pi} = -1$. The second term then implies that $j_{\mu z}$ describes particles with charge 1/2. Ultimately, the presence of a charge-1/2 semion is consistent with the expected result for a flux 2π vortex line. We also note that following $c_\mu = -a_\mu/2$ and Equation 5.28 we have:

$$\oint \nabla\theta \cdot d\ell = -\iint \nabla \times \boldsymbol{a} \cdot \boldsymbol{dS} \tag{5.33}$$

which implies that a vison excitation of the $\mathbb{Z}_2$ gauge field describes a flux π vortex. Hence the vortex current for flux π superconducting vortices is of the form $\frac{1}{\pi}\epsilon_{z\mu\nu\lambda}\partial_\nu a_\lambda$. Following the argument from [33], a flux π vortex line induces a Majorana zero mode. Such a vortex line can also be verified to induce a charge-1/4. Namely, substituting $c_\mu = -\frac{A_\mu + a_\mu}{2}$ into 5.27 gives:

$$\mathcal{L} = \mathcal{L}_f\left(-a_\mu\right) - \frac{i}{8\pi}\epsilon_{z\mu\nu\lambda} A_\mu \partial_\nu A_\lambda - \frac{i}{4\pi}\epsilon_{z\mu\nu\lambda} A_\mu \partial_\nu a_\lambda - \frac{i}{8\pi}\epsilon_{z\mu\nu\lambda} a_\mu \partial_\nu a_\lambda$$

which confirms that an odd flux vortex line induces charge-1/4.

5.4 Weyl Charge Density Wave State

We now consider an alternative construction to this $\mathbb{Z}_4$ topological order using charge density wave interactions. Once again, we begin the Hamiltonian for a gapless Weyl semimetal given in Equation 5.18. We add the following repulsive electron-electron interaction term:

$$H_{int} = U \sum_i \psi^\dagger_{i\uparrow}\psi^\dagger_{i\downarrow}\psi_{i\downarrow}\psi_{i\uparrow} = -\frac{U}{2}\sum_i \left(\psi^\dagger_i \sigma_z \psi_i\right)^2 \tag{5.34}$$

Decoupling this interaction term using a Hubbard-Stratonovich transformation gives the following imaginary-time action:

$$S = \int_0^\beta d\tau \left\{ \sum_{\mathbf{k}} \psi^\dagger_{\mathbf{k}} \left[\partial_\tau + H_0(\mathbf{k})\right] \psi_{\mathbf{k}} + \sum_i \left(\Delta_i \psi^\dagger_i \sigma_z \psi_i + \frac{\Delta_i^2}{2U} \right) \right\} \tag{5.35}$$

where the auxiliary field Δ_i is a charge density wave (CDW) order parameter [62]. We will take Δ_i to be of the form $\Delta_i = \Delta\cos\left(2\mathbf{Q}\cdot\mathbf{r}_i + \varphi\right)$ where $\boldsymbol{r}_i$ labels a lattice point. Substituting this form for Δ_i and applying the Fourier transform $\psi_i = \frac{1}{\sqrt{N}}\sum_k \psi_k e^{i\boldsymbol{k}\cdot\boldsymbol{r}_i}$ gives:

$$\begin{aligned} S &= \int_0^\beta d\tau \left(\sum_{\boldsymbol{k}} \psi^*_{\boldsymbol{k}} \left(\partial_\tau + H_0(\boldsymbol{k})\right) \psi_{\boldsymbol{k}} + \sum_i \left(\frac{\Delta}{2}\left[e^{i(2\boldsymbol{Q}\cdot\boldsymbol{r}_i+\varphi)} + e^{-i(2\boldsymbol{Q}\cdot\boldsymbol{r}_i+\varphi)} \right] \psi^*_i \sigma_z \psi_i + \frac{1}{2U}\Delta_i^2 \right) \right) \\ &= \int_0^\beta d\tau \left(\sum_{\boldsymbol{k}} \psi^*_{\boldsymbol{k}} \left(\partial_\tau + H_0(\boldsymbol{k})\right) \psi_{\boldsymbol{k}} + \frac{\Delta}{2}\sum_{\boldsymbol{k}} \left(\psi^*_{\boldsymbol{k}+2\boldsymbol{Q}} \sigma_z \psi_{\boldsymbol{k}} e^{i\varphi} + \psi^*_{\boldsymbol{k}} \sigma_z \psi_{\boldsymbol{k}+2\boldsymbol{Q}} e^{-i\varphi} \right) \right) \end{aligned}$$

With a Brillouin zone of $-Q \le k_z < Q$, we can rewrite the Hamiltonian as:

$$\begin{aligned} H &= \sum_{\boldsymbol{k}} c^\dagger_{\boldsymbol{k}} H_0(k) c_{\boldsymbol{k}} + \frac{\Delta}{2}\sum_{\boldsymbol{k}} \left(c^\dagger_{\boldsymbol{k}+2\boldsymbol{Q}} \sigma_z c_{\boldsymbol{k}} e^{i\varphi} + c^\dagger_{\boldsymbol{k}} \sigma_z c_{\boldsymbol{k}+2\boldsymbol{Q}} e^{-i\varphi} \right) \\ &= \frac{1}{2}\sum_{\boldsymbol{k}} c^\dagger_{\boldsymbol{k}+2\boldsymbol{Q}} H_0(\boldsymbol{k}+2\boldsymbol{Q}) c_{\boldsymbol{k}+2\boldsymbol{Q}} + \frac{1}{2}\sum_{\boldsymbol{k}} c^\dagger_{\boldsymbol{k}} H_0(k) c_{\boldsymbol{k}} + \frac{\Delta}{2}\sum_{\boldsymbol{k}} \left(c^\dagger_{\boldsymbol{k}+2\boldsymbol{Q}} \sigma_z c_{\boldsymbol{k}} e^{i\varphi} + c^\dagger_{k-2Q} \sigma_z c_{\boldsymbol{k}} e^{-i\varphi} \right) \\ &= \frac{1}{2}\sum_{\boldsymbol{k}} c^\dagger_{\boldsymbol{k}+2\boldsymbol{Q}} H_0(\boldsymbol{k}+2\boldsymbol{Q}) c_{\boldsymbol{k}+2\boldsymbol{Q}} + \frac{1}{2}\sum_{\boldsymbol{k}} c^\dagger_{\boldsymbol{k}} H_0(k) c_{\boldsymbol{k}} + \frac{\Delta}{2}\cos\varphi \sum_{\boldsymbol{k}} \left(c^\dagger_{\boldsymbol{k}+2\boldsymbol{Q}} \sigma_z c_{\boldsymbol{k}} + \text{h.c.} \right) \end{aligned}$$

Introducing spinor $\psi_k = (c_{k+2Q}, c_k)$ gives:

$$H = \sum_{\boldsymbol{k}} \left(\psi^\dagger_{\boldsymbol{k}} \frac{1}{2} \left(1 + \tau^z\right) H_0(\boldsymbol{k} + \boldsymbol{2Q}) \psi_{\boldsymbol{k}} + \psi^\dagger_{\boldsymbol{k}} \frac{1}{2} \left(1 - \tau^z\right) H_0(k) \psi_{\boldsymbol{k}} + \Delta \cos\varphi \psi^\dagger_{\boldsymbol{k}} \tau_x \sigma_z \psi_{\boldsymbol{k}} \right)$$

As in [33, 34], we assume a Weyl node separation of $2\boldsymbol{Q} = \pi\hat{\boldsymbol{z}}$. This gives:

$$H = \sum_{\boldsymbol{k}} \psi^\dagger_{\boldsymbol{k}} \left(\sigma_x \sin k_x + \sigma_y \sin k_y + \tilde{m} \left(2 - \cos k_x - \cos k_y\right) \sigma_z + \tau_z \sigma_z \cos k_z + \Delta \cos\varphi \tau_x \sigma_z \right) \psi_{\boldsymbol{k}}$$

Diagonalizing the coefficient of σ_z block gives a term of the form $m_\pm(\boldsymbol{k})\sigma^z$ where:

$$m_\pm(\boldsymbol{k}) = \tilde{m} \left(2 - \cos k_x - \cos k_y\right) \pm \sqrt{\cos^2 k_z + \Delta^2 \cos^2 \varphi}$$

Thus the band dispersion is given by $\varepsilon_{rs}(\boldsymbol{k}) = s\sqrt{\sin^2 k_x + \sin^2 k_y + m_r^2(\boldsymbol{k})}$ where $s, r = \pm$. It follows that $\varphi = 0$ and $\varphi = \pi$ are the energetically preferred values of the phase of the CDW order parameter, since the band gap is maximal for these cases.

5.4.1 Domain Wall States

We would now like to find the analytical solution for the domain wall bound state between the two CDW ground states: $\varphi = 0$ and $\varphi = \pi$. Namely, we consider a scenario in which $\varphi(z \to -\infty) = \pi$ and $\varphi(z \to \infty) = 0$. Since the band gap closes at $\varphi = \pi/2$, we expect a zero energy state to be localized at the interface. Beginning with the Hamiltonian in Equation 5.4, we apply a unitary rotation in τ space such that $\tau_y \to -\tau_z$ and $\tau_z \to \tau_y$. This gives:

$$H = \sum_{k} \psi^\dagger_{k} \left(\sigma_x \sin k_x + \sigma_y \sin k_y + \tilde{m} \left(2 - \cos k_x - \cos k_y\right) \sigma_z + \tau_y \sigma_z \cos k_z + \Delta \cos\varphi \tau_x \sigma_z \right) \psi_{k}$$

Then applying the canonical transformation $\tau^\pm \to \sigma_z \tau^\pm$ and $\sigma^\pm \to \tau_z \sigma^\pm$ gives:

$$H = \sum_{k} \psi^\dagger_{k} \left(\sigma_x \tau_z \sin k_x + \sigma_y \tau_z \sin k_y + \tilde{m} \left(2 - \cos k_x - \cos k_y\right) \sigma_z + \tau_y \cos k_z + \Delta \cos\varphi \tau_x \right) \psi_{k}$$

Taylor expanding the $\cos k_z$ term to linear order around $k_z = \pi/2$ gives $\cos k_z \to i\partial_z$. Then assuming $k_x = k_y = 0$ gives:

$$H(k) = i\tau_y \frac{\partial}{\partial z} + \Delta \cos\varphi \tau_x$$

We would like to solve for the zero energy state $H\psi = 0$, which we expect to be localized at the interface between the two phases. Let us assume $\psi(z) = \tau_y e^{f(z)}|x\rangle$. Then we have:

$$\left(i\tau_y \frac{\partial}{\partial z} + \Delta \cos\varphi \tau_x\right) e^{f(z)}\tau_y|x\rangle = 0 \Rightarrow \left(\frac{\partial f}{\partial z} + \tau_z \Delta \cos\varphi\right)|x\rangle = 0$$

where we choose $\tau_z|x\rangle = |x\rangle$. Hence it follows that $f(z) = -\Delta \int_0^z dz' \cos\varphi(z')$. From $\tau_z|x\rangle = |x\rangle$ it also follows that $\tau_z\tau_y|x\rangle = -\tau_y\tau_z|x\rangle = -\tau_y|x\rangle$. Thus we ultimately have:

$$\psi(z) = \exp\left(-\Delta \int_0^z dz' \cos\varphi(z')\right)|\tau_z = -1\rangle$$

Hence, our zero energy state is indeed localized at $z = 0$. By this construction we have:

$$\begin{aligned} H_{2D}(\boldsymbol{k})\psi(z) &= \left[\sigma_x\tau_z \sin k_x + \sigma_y\tau_z \sin k_y + \tilde{m}(2 - \cos k_x - \cos k_y)\sigma_z\right]\psi(z) \\ &= \left[-\sigma_x \sin k_x - \sigma_y \sin k_y + \tilde{m}(2 - \cos k_x - \cos k_y)\sigma_z\right]\psi(z) \end{aligned}$$

Thus the Hamiltonian for our domain wall bound state takes the form of a massless 2D Dirac fermion:

$$H_{2D}(\boldsymbol{k}) = -\sigma_x \sin k_x - \sigma_y \sin k_y + \tilde{m}(2 - \cos k_x - \cos k_y)\sigma_z \tag{5.36}$$

5.4.2 $\mathbb{Z}_4$ Topological Order

Now let us take the 2D Dirac Hamiltonian from Equation 5.36 and consider applying the same vortex condensation procedure as in the construction of the hydrodynamic BF theory. Fourier transforming to real space and coupling to an external electromagnetic field gives:

$$H = \sum_{\mathbf{r}} \left[\frac{i}{2}\psi_{\mathbf{r}}^\dagger(\sigma_i - i\tilde{m}\sigma_z)\psi_{\mathbf{r}+i}e^{iA_{\mathbf{r}i}} + h.c. - 2\tilde{m}\psi_{\mathbf{r}}^\dagger\sigma_z\psi_{\mathbf{r}} + iA_{\mathbf{r}0}\psi_{\mathbf{r}}^\dagger\psi_{\mathbf{r}}\right]$$

Once again, we consider the parton representation $\psi_{\boldsymbol{r}} = e^{i\theta_{\boldsymbol{r}}} f_{\boldsymbol{r}}$ and decouple the two variables using a Hubbard-Stratonovich transformation to obtain $\mathcal{L} = \mathcal{L}_f + \mathcal{L}_b$ where:

$$\mathcal{L}_f = f^\dagger_{\mathbf{r}} \left(\partial_\tau - i a_{\mathbf{r}0}\right) f_{\mathbf{r}} - 2\tilde{m} f^\dagger_{\mathbf{r}} \sigma_z f_{\mathbf{r}} + \frac{i\chi}{2} f^\dagger_{\mathbf{r}} \left(\sigma_i - i\tilde{m}\sigma_z\right) f_{\mathbf{r}+i} e^{-i a_{\mathbf{r}i}} + h.c. \tag{5.37}$$

$$\mathcal{L}_b = i n_{\mathbf{r}} \left(\partial_\tau \theta_{\mathbf{r}} + A_{\mathbf{r}0} + a_{\mathbf{r}0}\right) - \chi \cos\left(\Delta_i \theta_{\mathbf{r}} + A_{\mathbf{r}i} + a_{\mathbf{r}i}\right) \tag{5.38}$$

where $a_{\boldsymbol{r}\mu}$ is the phase of the Hubbard-Stratonovich field and couples the chargons and spinons. Exactly as before, we add a BCS term to the spinon Hamiltonian to obtain:

$$\begin{aligned} H &= -\sum_{\mathbf{k}} f^\dagger_{\mathbf{k}} \left[\chi\sigma_x \sin\left(k_x\right) + \chi\sigma_y \sin\left(k_y\right) + \sigma_z m(\mathbf{k})\right] f_{\mathbf{k}} - \Delta \sum_{\mathbf{k}} \left(f^\dagger_{\mathbf{k}\uparrow} f^\dagger_{-\mathbf{k}\downarrow} + f_{-\mathbf{k}\downarrow} f_{\mathbf{k}\uparrow}\right) \\ &= -\frac{1}{2} \sum_{\mathbf{k}} \tilde{f}^\dagger_{\mathbf{k}} \left\{\chi\sigma_x \sin\left(k_x\right) + \chi\sigma_y \sin\left(k_y\right) + [m(\mathbf{k}) \pm \Delta]\sigma_z\right\} \tilde{f}_{\mathbf{k}} \end{aligned}$$

where $\tilde{f}_{\mathbf{k}} = \left(f_{\mathbf{k}\uparrow}, f_{\mathbf{k}\downarrow}, f^\dagger_{-\mathbf{k}\downarrow}, f^\dagger_{-\mathbf{k}\uparrow}\right)$. This describes a topological superconductor with a chiral Majorana edge mode and a zero-energy Majorana bound state in the $hc/2e = \pi$-flux core [58, 59]. Next we consider the charge sector of the theory. Decoupling the cosine using a Villain transformation gives:

$$\mathcal{L}_b = i J_{\mathbf{r}\mu} \left(\Delta_\mu \theta_{\mathbf{r}} + A_{\mathbf{r}\mu} + a_{\mathbf{r}\mu}\right) + \frac{1}{2\chi} J^2_{\mathbf{r}\mu} \tag{5.39}$$

where $J_{\boldsymbol{r}\mu}$ are integer chargon currents defined on the links of the lattice. Integrating out $\theta_{\boldsymbol{r}}$ produces a conservation law for the chargon currents:

$$\Delta_\mu J_{\mathbf{r}\mu} = 0$$

which may be solved as:

$$J_\mu = \frac{1}{2\pi} \epsilon_{\mu\nu\lambda} \Delta_\nu b_\lambda$$

where $b_\mu \in 2\pi\mathbb{Z}$ are defined on the links of the dual lattice. This constraint can be relaxed by introducing a cosine term:

$$\mathcal{L}_b = \frac{i}{2\pi}\left(A_\mu + a_\mu\right)\epsilon_{\mu\nu\lambda}\Delta_\nu b_\lambda + \frac{1}{8\pi^2\chi}\left(\epsilon_{\mu\nu\lambda}b_\lambda\right)^2 - t\cos\left(\Delta_\mu\phi + b_\mu\right) \tag{5.40}$$

To describe the condensation of flux 4π vortices, we consider modifying the cosine term to be $-t\cos(2\Delta_\mu\phi + 2b_\mu)$. Applying another Villain transformation to decouple this cosine term gives:

$$\mathcal{L}_b = \frac{i}{2\pi}\left(A_\mu + a_\mu\right)\epsilon_{\mu\nu\lambda}\Delta_\nu b_\lambda + \frac{1}{8\pi^2\chi}\left(\epsilon_{\mu\nu\lambda}b_\lambda\right)^2 + 2i\tilde{J}_\mu\left(\Delta_\mu\phi + b_\mu\right) + \frac{1}{2t}\tilde{J}_\mu^2$$

where $\tilde{J}_\mu$ are integer vortex currents. Integrating out ϕ produces a vorticity conservation law of the form $\Delta_\mu\tilde{J}_\mu = 0$ which may be solved as

$$\tilde{J}_\mu = \frac{1}{2\pi}\epsilon_{\mu\nu\lambda}\Delta_v\tilde{b}_\lambda$$

where $\tilde{b}_\mu \in 2\pi\mathbb{Z}$. Adding a Chern-Simons term for $\tilde{b}_\mu$ and taking the continuum limit:

$$\mathcal{L}_b = \frac{i}{2\pi}\left(A_\mu + a_\mu + 2\tilde{b}_\mu\right)\epsilon_{\mu\nu\lambda}\partial_\nu b_\lambda - \frac{2i}{4\pi}\epsilon_{\mu\nu\lambda}\tilde{b}_\mu\partial_\nu\tilde{b}_\lambda \tag{5.41}$$

which possesses the same responses as Equation 5.27. Namely, the same flux attachment calculation used above demonstrates that flux 2π vortices induce charge-1/2 semions. Furthermore, integrating out b_μ gives:

$$\tilde{b}_\mu = -\frac{A_\mu + a_\mu}{2}$$

Plugging this back into the full Lagrangian gives:

$$\mathcal{L} = \mathcal{L}_f\left(-a_\mu\right) - \frac{i}{8\pi}\epsilon_{\mu\nu\lambda}A_\mu\partial_\nu A_\lambda - \frac{i}{4\pi}\epsilon_{\mu\nu\lambda}A_\mu\partial_\nu a_\lambda - \frac{i}{8\pi}\epsilon_{\mu\nu\lambda}a_\mu\partial_\nu a_\lambda \tag{5.42}$$

which implies that visons and hence odd flux vortex loops carry charge 1/4 in addition to Majorana zero modes. Ultimately, Equation 5.41 can be generalized to 3D by promoting the one-form gauge field b_μ to a two-form gauge field $b_{\mu\nu}$. This expresses the fact that vortex excitations, which are particles in 2D, becomes vortex loops in 3D.

5.5 Edge Theory

In this section, our goal will be derive the edge theory of the BF theory given in Equation 5.27. As reviewed in Section 5.3.1, the one-form gauge field c_μ and the two-form gauge field $b_{\mu\nu}$ possess gauge transformations $c_\mu \to c_\mu + \partial_\mu f$ and $b_{\mu\nu} \to b_{\mu\nu} + \partial_\mu g_\nu - \partial_\nu g_\mu$. One can verify that the Lagrangian given in Equation 5.27 is indeed invariant under these transformations. Namely, the Lagrangian would acquire the following additional terms:

$$\Delta\mathcal{L} = \frac{i}{2\pi}\epsilon_{\mu\nu\lambda\rho}\partial_\mu\left(f\partial_\nu b_{\lambda\rho}\right) + \frac{i}{\pi}\epsilon_{\mu\nu\lambda\rho}\partial_\mu\left(g_\nu\partial_\lambda c_\rho\right) + \frac{i}{2\pi}\epsilon_{\mu\nu\lambda\rho}\partial_\mu\left(z_\nu f\partial_\lambda c_\rho\right)$$

which vanish upon integration. However, this invariance no longer holds under the presence of a boundary. Namely, the contribution of $\Delta\mathcal{L}$ becomes non-vanishing. Following the approach of Wen for the 2D FQH liquid [35], which is described by a 2+1D Chern-Simons term, we recognize that gauge invariance can be restored by explicitly gauge-fixing on the boundary: $c_0 = 0$ and $b_{0\mu} = 0$. Now let us derive the resulting edge theory. Beginning with the BF term:

$$\begin{aligned}
S_{\text{BF}} &= \frac{i}{2\pi}\int_0^\beta d\tau \int d^3r \epsilon^{\mu\nu\lambda\rho} c_\mu \partial_\nu b_{\lambda\rho} \\
&= \frac{i}{2\pi}\int_0^\beta d\tau \int d^3r (c_0(\partial_x(b_{yz} - b_{zy}) + \partial_y(b_{zx} - b_{xz}) + \partial_z(b_{xy} - b_{yz})) \\
&+ c_x(\partial_\tau(b_{zy} - b_{yz}) + \partial_y(b_{0z} - b_{z0}) + \partial_z(b_{y0} - b_{0y})) \\
&+ c_y(\partial_\tau(b_{xz} - b_{zx}) + \partial_x(b_{z0} - b_{0z}) + \partial_z(b_{0x} - b_{x0})) \\
&+ c_z(\partial_\tau(b_{yx} - b_{xy}) + \partial_x(b_{0y} - b_{y0}) + \partial_y(b_{x0} - b_{0x}))
\end{aligned}$$

Integrating out c_0 gives $\epsilon_{ijk}\partial_i b_{jk} = 0$ which can be solved as $b_{ij} = \epsilon_{ij}\partial_i g_j$. Next we note:

$$\begin{aligned}
-c_x(\partial_y b_{z0} - \partial_z b_{y0}) &= -(\partial_y(c_x b_{z0}) - b_{z0}\partial_y c_x) + (\partial_z(c_x b_{y0}) - b_{y0}\partial_z c_x) \\
+c_y(\partial_x b_{z0} - \partial_z b_{x0}) &= +(\partial_x(c_y b_{z0}) - b_{z0}\partial_x c_y) - (\partial_z(c_y b_{x0}) - b_{x0}\partial_z c_y) \\
-c_z(\partial_x b_{y0} - \partial_y b_{x0}) &= -(\partial_x(c_z b_{y0}) - b_{y0}\partial_x c_z) + (\partial_y(c_z b_{x0}) - b_{x0}\partial_y c_z)
\end{aligned}$$

Integrating out total derivatives and noting that the ∂_y terms cancel since we fixed $b_{0i} = 0$ on the boundary, these terms simplify to $-b_{x0}(\partial_y c_z - \partial_z c_y) + b_{y0}(\partial_x c_z - \partial_z c_x) -$

$b_{z0}(\partial_x c_y - \partial_y c_x)$. Hence integrating out b_{0i} gives $\epsilon_{ij}\partial_i c_j = 0$ which can be solved as $c_i = \partial_i \varphi$. Then finally we have:

$$\begin{aligned}
S &= \frac{1}{2\pi}\int d^4x\,(c_x\partial_\tau(b_{zy}-b_{yz}) + c_y\partial_\tau(b_{xz}-b_{zx}) + c_z\partial_\tau(b_{yx}-b_{xy})))\\
&= \frac{1}{2\pi}\int d^4x\,(\partial_x\varphi\partial_\tau(\partial_z g_y - \partial_y g_z) + \partial_y\varphi\partial_\tau(\partial_x g_z - \partial_z g_x) + \partial_z\varphi\partial_\tau(\partial_y g_x - \partial_x g_y)))\\
&= \frac{1}{2\pi}\int d^4x\,(\partial_x\left(\varphi\partial_\tau(\partial_z g_y - \partial_y g_z)\right) + \partial_y\left(\varphi\partial_\tau(\partial_x g_z - \partial_z g_x)\right) + \partial_z\left(\varphi\partial_\tau(\partial_y g_x - \partial_x g_y)\right))\\
&\qquad - \varphi\left(\partial_x\partial_\tau(\partial_z g_y - \partial_y g_z) + \partial_y\partial_\tau(\partial_x g_z - \partial_z g_x) + \partial_z\partial_\tau(\partial_y g_x - \partial_x g_y)\right)\\
&= \frac{1}{2\pi}\int_{y=0} d^3x\varphi\partial_\tau(\partial_x g_z - \partial_z g_x)
\end{aligned}$$

Following a final integration by parts, we obtain the following contribution to our boundary Lagrangian from the BF term:

$$\mathcal{L}_{\mathrm{BF}} = -\frac{\epsilon_{ij}}{2\pi}\partial_\tau\varphi\partial_i g_j \tag{5.43}$$

Now let us consider the Chern-Simons action:

$$\begin{aligned}
S_{\mathrm{CS}} &= -\frac{i}{2\pi}\int_0^\beta d\tau\int d^3r\epsilon^{\mu\nu\lambda\rho}z_\mu c_\nu\partial_\lambda c_\rho\\
&= -\frac{i}{2\pi}\int_0^\beta d\tau\int d^3r c_0\,(z_x(\partial_y c_z - \partial_z c_y) + z_y(\partial_z c_x - \partial_x c_z) + z_z(\partial_x c_y - \partial_y c_x))\\
&\quad + c_x\,(z_0(\partial_z c_y - \partial_y c_z) + z_y(\partial_t c_z - \partial_z c_0) + z_z(\partial_y c_0 - \partial_t c_y))\\
&\quad + c_y\,(z_0(\partial_x c_z - \partial_z c_x) + z_x(\partial_z c_0 - \partial_t c_z) + z_z(\partial_t c_x - \partial_x c_0))\\
&\quad + c_z\,(z_0(\partial_y c_x - \partial_x c_y) + z_x(\partial_t c_y - \partial_y c_0) + z_y(\partial_x c_0 - \partial_t c_x))
\end{aligned}$$

where the translational gauge field z_μ allows for a coordinate-independent formulation. Integrating out c_0 gives $c_i = \partial_i\varphi$ as above. This holds, since all terms containing spatial derivatives of c_0 simply contribute to the first line of terms. For example, $c_x z_z \partial_y c_0$ becomes:

$$c_x z_z\partial_y c_0 = \partial_y(c_x z_z c_0) - c_0\partial_y(c_x z_z) = \partial_y(c_x z_z c_0) - c_0(c_x\partial_y z_x - z_z\partial_y c_x)$$

where the first term cancels since we fixed $c_0 = 0$ on the boundary and the second term cancels since we assume $dz = 0$. Substituting $c_i = \partial_i \varphi$ into the remaining terms and integrating by parts gives:

$$\begin{aligned} S_{\text{CS}} &= -\frac{i}{2\pi} \int d^4x \partial_x \varphi (z_y \partial_\tau \partial_z \varphi - z_z \partial_\tau \partial_y \varphi) + \partial_y \varphi (z_z \partial_\tau \partial_x \varphi - z_x \partial_\tau \partial_z \varphi) + \partial_z \varphi (z_x \partial_\tau \partial_y \varphi - z_y \partial_\tau \partial_x \varphi) \\ &= -\frac{i}{2\pi} \int d^4x \partial_y (z_x \partial_z \varphi \partial_\tau \varphi - z_z \partial_x \varphi \partial_\tau \varphi) \end{aligned}$$

where we note that the additional terms $z_x(\partial_y \partial_z \varphi - \partial_z \partial_y \varphi) + z_y(\partial_z \partial_x \varphi - \partial_x \partial_z \varphi) + z_z(\partial_x \partial_y \varphi - \partial_y \partial_x \varphi)$ resulting from integrating by parts all cancel. This gives the following boundary Lagrangian:

$$\mathcal{L}_{\text{CS}} = \frac{i}{2\pi} \epsilon_{ij} z_i \partial_\tau \varphi \partial_j \varphi \tag{5.44}$$

Overall our surface state Lagrangian is given by:

$$\mathcal{L} = \mathcal{L}_{\text{CS}} + \mathcal{L}_{\text{BF}} = \frac{i}{2\pi} \epsilon_{ij} z_i \partial_\tau \varphi \partial_j \varphi - \frac{i}{2\pi} \epsilon_{ij} \partial_\tau \varphi \partial_i g_j \tag{5.45}$$

Let us confirm that this edge theory Lagrangian produces an electrical response that is consistent with the bulk. To begin, we add a coupling term for the external electromagnetic field:

$$\mathcal{L} = \frac{i}{2\pi} \epsilon_{ij} z_i \partial_\tau \varphi \partial_j \varphi - \frac{i}{\pi} \epsilon_{ij} \partial_\tau \varphi \partial_i g_j + \frac{i}{2\pi} \epsilon_{\mu\nu\lambda} A_\mu \partial_\nu g_\lambda \tag{5.46}$$

Varying with respect to φ gives $\epsilon_{ij} \partial_\tau \partial_i (z_j \varphi + g_j) = 0$ and hence $g_i = -z_i \varphi$. On the other hand, varying with respect to g_i gives $\epsilon_{ij} \partial_j (\partial_\tau \varphi - A_0/2) = 0$ which implies $\partial_\tau \varphi = A_0/2$. From the coupling term for the electromagnetic gauge field, we also have that:

$$\rho = -\frac{1}{2\pi} \epsilon_{ij} \partial_i g_j = -\frac{1}{2\pi} z_i \epsilon_{ij} \partial_j \varphi \tag{5.47}$$

following $g_i = -z_i \varphi$. Then acting $\frac{1}{2\pi} z_i \epsilon_{ij} \partial_j$ on both sides of $\partial_\tau \varphi = A_0/2$ gives:

$$\partial_\tau \rho = -\frac{1}{4\pi} z_i \epsilon_{ij} \partial_j A_0 \tag{5.48}$$

This is the chiral anomaly equation for an electrical Hall conductance of $\sigma_{xy} = 1/4\pi$.

5.5.1 Propagator

We would now like to study the properties of this edge theory. In the case of the 2D FQH liquid, doing so requires the addition of a symmetry-allowed term of the form $v(\partial_x\varphi)^2$. With this term, the resulting electron propagator for a Laughlin state with $\nu = 1/m$ takes the form of a chiral Luttinger liquid [35]:

$$\mathcal{G}(x,t) = \left\langle \Psi(x,t)\Psi^\dagger(0,0)\right\rangle \sim \frac{1}{(x+vt)^m} \tag{5.49}$$

where $\Psi = e^{im\varphi}$ is the electron operator. This describes a chiral wave propagating with speed v along the boundary. The symmetry-allowed term $v(\partial_x\varphi)^2$ can in fact be derived explicitly be generalizing the gauge-fixing condition to be $c_t = vc_x$ at the boundary and considering a change of coordinates [36]. For our edge theory described in Equation 5.45, which includes the one-form field g_i, we consider an additional symmetry-allowed term of the form $(\epsilon_{ij}\partial_i g_j)^2$. Ultimately, we write our full edge theory Lagrangian as:

$$\mathcal{L} = \frac{i}{2\pi}\epsilon_{ij}z_i\partial_\tau\varphi\partial_j\varphi - \frac{i}{\pi}\epsilon_{ij}\partial_\tau\varphi\partial_i g_j + v_\varphi\left(\partial_i\varphi\right)^2 + v_g\left(\partial_i g_j - \partial_j g_i\right)^2 \tag{5.50}$$

Integrating out g_i gives:

$$\mathcal{L} = \frac{i}{2\pi}\epsilon_{ij}z_i\partial_\tau\varphi\partial_j\varphi + v_\varphi\left(\partial_i\varphi\right)^2 + \frac{1}{4\pi^2 v_g}(\partial_\tau\varphi)^2 \tag{5.51}$$

For our original case of $z_x = 0$ and $z_z = 1$, this reduces to:

$$\mathcal{L} = \frac{i}{2\pi}\partial_\tau\varphi\partial_x\varphi + v_\varphi\left(\partial_i\varphi\right)^2 + \frac{1}{4\pi^2 v_g}(\partial_\tau\varphi)^2 \tag{5.52}$$

To compute the propagator, we need the Green's function for the field φ:

$$\begin{aligned} S &= \int d^3x \frac{i}{2\pi}\partial_\tau\varphi\partial_x\varphi + v_\varphi\left(\partial_i\varphi\right)^2 + \frac{1}{4\pi^2 v_g}(\partial_\tau\varphi)^2 \\ &= \sum_{\boldsymbol{q}\Omega}\left(\frac{i}{2\pi}q_x\Omega - v_\varphi|\boldsymbol{q}|^2 - \frac{1}{4\pi^2 v_g}\Omega^2\right)\varphi(\boldsymbol{q},\Omega)\varphi(-\boldsymbol{q},-\Omega) \\ &= \sum_{\boldsymbol{q}\Omega}\mathcal{G}_\varphi^{-1}(\boldsymbol{q},i\Omega)\varphi(\boldsymbol{q},\Omega)\varphi(-\boldsymbol{q},-\Omega) \end{aligned}$$

Hence, the real-space Green's function for φ is given by:

$$\mathcal{G}_\varphi(x,z,\tau) = 4\pi^2 \int dq_x dq_z d\Omega \frac{e^{i(\boldsymbol{q}\cdot\boldsymbol{x}-\Omega\tau)}}{a\Omega^2+b\Omega+c} \tag{5.53}$$

where $a \equiv -1/v_g$, $b \equiv 2\pi i q_x$, and $c \equiv -4\pi^2 v_\varphi |\boldsymbol{q}|^2$. To compute the integral over Ω, we can simply complete the square and compute the shifted inverse Fourier transform of $\frac{1}{x^2+a^2}$. Namely we have:

$$\mathcal{G}_\varphi(x,z,\tau) = \frac{4\pi^2}{a} \int dq_x dq_z d\Omega \frac{e^{i(\boldsymbol{q}\cdot\boldsymbol{x}-\Omega\tau)}}{(\Omega+A)^2+B} \tag{5.54}$$

$$\tag{5.55}$$

where $A = \frac{b}{2a}$ and $B = \frac{c}{a} - \frac{b^2}{4a^2}$. The shifted inverse Fourier transform is given by:

$$\int \frac{e^{-i\Omega\tau}}{(\Omega+A)^2+B} d\Omega = e^{iA\tau} \frac{\pi}{\sqrt{B}} e^{-\sqrt{B}|\tau|} \tag{5.56}$$

And hence the propagator evaluates as:

$$\begin{aligned}
\mathcal{G}_\varphi(x,z,\tau) &= \frac{4\pi^2}{a} \int dq_x dq_z e^{i\boldsymbol{q}\cdot\boldsymbol{x}} e^{iA\tau} \frac{\pi}{\sqrt{B}} e^{-\sqrt{B}\tau} \\
&= -4\pi^2 \int dq_x dq_z \frac{e^{i\boldsymbol{q}\cdot\boldsymbol{x}} e^{\pi v_g q_x \tau} e^{-\pi v_g \sqrt{q_x^2 + v|\boldsymbol{q}|^2}\tau}}{\sqrt{q_x^2 + v|\boldsymbol{q}|^2}} \\
&= -4\pi^2 \int dq_x dq_z \frac{e^{i\boldsymbol{q}\cdot\boldsymbol{x}} e^{\pi v_g q_x \tau} e^{-\pi v_g \sqrt{(1+v)q_x^2 + vq_z^2}\tau}}{\sqrt{(1+v)q_x^2 + vq_z^2}}
\end{aligned}$$

where $v \equiv \frac{4v_\varphi}{v_g}$. In the $q_z = 0$ case, this simplifies to:

$$\begin{aligned}
\mathcal{G}_\varphi(x,\tau) &= -4\pi^2 \int dq_x \frac{e^{iq_x x + \pi v_g(q_x - \sqrt{1+v}|q_x|)\tau}}{\sqrt{1+v}|q_x|} \\
&= -\frac{8\pi^3}{L}\frac{1}{\sqrt{1+v}} \sum_{q_x>0} \frac{\left(e^{ix+\pi v_g(1-\sqrt{1+v})\tau}\right)^{q_x}}{q_x} \\
&= -\frac{8\pi^3}{L}\frac{1}{\sqrt{1+v}}\frac{L}{2\pi} \sum_{n_x>0} \frac{\left(e^{2\pi(ix+\pi v_g(1-\sqrt{1+v})\tau)/L}\right)^{n_x}}{n_x} \\
&= -\frac{4\pi^2}{\sqrt{1+v}} \ln\left(1 - e^{\frac{2\pi(ix+\pi v_g(1-\sqrt{1+v})\tau)}{L}}\right)
\end{aligned}$$

where we have chosen $q_x > 0$. We can expand to first order if we assume $x \ll L$ and $\tilde{v}|t| \ll L$ where $\tilde{v} := \pi v_g(1 - \sqrt{1+v})$:

$$\mathcal{G}_\varphi(x,\tau) = -\frac{4\pi^2}{\sqrt{1+v}} \ln\left(-\frac{2\pi(ix+\tilde{v}\tau)}{L}\right) = -\frac{4\pi^2}{\sqrt{1+v}} \ln\left(\frac{x - i\tilde{v}\tau}{L}\right) + \text{CST}$$

Hence, the propagator for our charge operator $\Psi(r,\tau) = e^{i\varphi}$ is given by:

$$\begin{aligned}
\mathcal{G}(r-r', \tau-\tau') &= \langle \Psi(r,\tau)\Psi^\dagger(r',\tau')\rangle \\
&= e^{-\mathcal{G}_\varphi(0,0)} e^{\mathcal{G}_\varphi(r-r',\tau-\tau')} \\
&= e^{-\mathcal{G}_\varphi(0,0)} \left(\frac{L}{(x-x') - i\tilde{v}(\tau-\tau')}\right)^{\frac{4\pi^2}{\sqrt{1+v}}}
\end{aligned}$$

Ultimately, this shows that the edge theory for the BF theory described in Equation 5.27 behaves as a chiral Luttinger liquid along the x direction. Namely, for correlations strictly along the x direction, the charge propagator reduces to $\mathcal{G}(x,t) \sim \frac{1}{(x+\tilde{v}t)^m}$ where $m = \frac{4\pi^2}{\sqrt{1+v}}$. Based on this observation, we anticipate that the full surface theory behaves as a stack of chiral Luttinger liquids that are coupled along the z direction. Ultimately, developing a deeper understanding of the properties of this surface theory is left as a problem for future work.

Chapter 6

Conclusions and Outlook

6.1 Detecting Topological Order

6.1.1 Summary of Chapters 3 and 4

In Chapter 2, we reviewed two of the defining features of topological order, namely quasi-particle excitations with non-trivial braiding and topological degeneracy, in the context of the toric code and general $\mathbb{Z}_2$ string liquids. In the case of the toric code, the quasi-particle excitations are defined by star and plaquette operators with negative parities, which are referred to as e and m particles, and possess mutual semion statistics. Furthermore, the topological degeneracy is 4-fold: there exists 4 distinct topological sectors differing by the presence of non-contractible strings of down spins. Ultimately, these properties are a manifestation of the local $\mathbb{Z}_2$ symmetries defining the model. The presence of such local symmetries forbids the existence of a local order parameter by Elitzur's theorem. One can however define the Wegner-Wilson and 't Hooft loop observables, which are invariant under these local symmetries, and exhibit transitions between perimeter and area laws with the tuning of external field parameters.

We consider identifying the topological degeneracy, loop structures and topological phase transition in the Wegner-Wilson loop using σ^z configurations sampled from the classical $\mathbb{Z}_2$ gauge theory using a Monte Carlo algorithm. In Chapter 3, we consider an implementation of the diffusion map algorithm to identify this topological degeneracy by clustering spin configurations according to their topological sector. Such an idea was first proposed and successfully implemented for the 2-dimensional case of the classical $\mathbb{Z}_2$ gauge theory in [22]. We show that this implementation is successful in the 3-dimensional

case, and we additionally show that a diffusion map analysis can successfully identify the location of the topological phase transition, namely the perimeter to area law transition in the Wegner-Wilson loop, as a peak in the *ch* metric, which compares the average size of clusters to the average distance between clusters. The use of a *ch* metric for identifying topological phase transitions following a diffusion map analysis was first considered in [23] in the context of XY models.

In Chapter 4, we consider the application of the Vietoris-Rips (VR) complex construction and persistent homology to the same Monte Carlo configurations, which is motivated by the interpretation of the $\mathbb{Z}_2$ gauge theory in the topologically ordered regime as a loop or *string-net* condensate [16, 17, 6]. The VR complex construction can be understood as a mapping of Ising configurations to geometric complexes of simplices. We show that the resulting first Betti number is indeed largest in the loop condensate phase, and hence propose the first Betti number of VR complexes as a new signature for topological order. In the 3-dimensional model, we show that this quantity is additionally successful in identifying the topological critical point, and is consistent with a functional form $(T - T_c)^{\phi}$ with an exponent $\phi \approx 0.544$. Rather than using the persistent homology analysis to identify this critical point following a machine learning classification [29, 30, 31, 32], we simply emphasis persistent homology as a tool for interpreting and distinguishing the various loop structures that form in topologically ordered regime.

6.1.2 Comparison of Approaches

From the machine learning perspective, both the diffusion map and persistent homology analysis have several advantages in comparison to neural network classification for the identification of phase transitions. Namely, both approaches are *unsupervised* in that no pre-labelling of the training data is required, and additionally do not possess any learning parameters or hyper-parameters. Hence, there is no parameter complexity, and no required tuning or hyper-parameter grid search. In regards to the sample complexity, we note that that the preliminary gauge-matching step in the diffusion map algorithm possesses a heavy bottleneck. Namely, the total number of computations for distances between spin configurations scales as $\mathcal{O}(M^2 N_G)$, where M is the total number of spin configurations and N_G is the total number of proposals required for the evaluation of a single element of the kernel matrix. On the other hand, we expect that the minimum number of samples required to correctly identify the phase transition in the homology computation of the first Betti number decays as $1/L^3$ for lattices with $N = D \times L^D$ degrees of freedom, since the first Betti number is shown to be extensive to a very good approximation.

We note that while the diffusion map algorithm is unsupervised, computation of the kernel matrix still requires knowledge of the local symmetry defining the model due to the preliminary gauge-matching step. Knowledge of the local symmetry is also required in the construction of any non-local order parameter used to identify the topological order. In contrast, computation of the first Betti number of the VR complex requires no previous knowledge of the system, and is completely interpretable. Namely, a general persistent homology analysis will allow one to identify and distinguish the various loop structures in any given configuration based on their corresponding birth and death values, with no previous knowledge of the gauge structure underlying the model.

6.1.3 Outlook for Diffusion Map Analysis

While it is true that the metric defined for the diffusion map algorithm requires knowledge of the local $\mathbb{Z}_2$ symmetry due to the preliminary gauge-matching step, there has been recent work on using machine learning algorithms to learn gauge symmetries [63, 64]. Hence, it may be possible to design an algorithm that can detect topological degeneracy without the need for any pre-existing knowledge of the physical system. Namely, an unsupervised learning algorithm could be used to first identify the local symmetry defining the topological order, which could in turn be used in the construction of the kernel for the diffusion map algorithm. In regards to the bottleneck, it was noticed both in our calculations and in the pre-existing work [22] that the number of required proposals for gauge-matching is at least on the order of 10^3 for minimal system sizes of $N = 6 \times 6 \times 2$. It may be possible to reduce the number of proposals and hence reduce the bottleneck by implementing a reinforcement learning agent [65, 66], with the objective of minimizing the Euclidean distance between any two spin configurations in the smallest number of proposals.

6.1.4 Outlook for Persistent Homology Analysis

One future model of interest would be the toric code with external field terms $h_X \sum \sigma^x$ and $h_Z \sum \sigma^z$, which can be mapped to the classical $3D$ $\mathbb{Z}_2$ gauge theory with a uniform field [67]. Such a model possesses two distinct deconfinement transitions characterized by the condensation of e particles (for $h_X \gg 1$) and m particles (for $h_Z \gg 1$). In the 2+1D membrane picture and the σ^x basis, h_X can be viewed as a parameter for the surface tension of membranes (since $\sum \sigma^x$ is a string tension term) and h_Z can be viewed as a parameter for the frequency of holes in the membranes (since $\sum \sigma^z$ is a generator for pairs of e particles) [68]. In this case, we expect that the frequency and persistence values

for H_1 and H_2 homologies may serve as useful tools for detecting and distinguishing the deconfinement transitions.

It would of additional interest to explore the behaviour of these Betti numbers in phase transitions not characterized by anyon condensation. One example would be the Haldane phase with hidden $\mathbb{Z}_2 \times \mathbb{Z}_2$ symmetry breaking [69]. The prominent structure of this nontrivial symmetry-protected topological (SPT) phase is closed strings of +1 and -1 spins, as defined by the string order parameter of den Nijs and Rommelse [70]. Another example would be the transitions between SPT phases and their gauge theory duals. For example, the transition between the toric code and double semion ground states was studied in [71] and was shown to possess stripe order. Here, we expect $\langle b_1 \rangle$ to be minimal at the center of the stripe order transition.

Finally, we note that all of the discussion so far has been based on geometric complex constructions and persistent homology of individual spin configurations. It is however possible to apply the same analysis to the configuration space, where each point in the construction of the geometric complex would represent one spin configuration in the Monte Carlo sampling. Such an idea was considered in [28] in the context of the mean-field XY model and lattice ϕ^4 model. One idea would be to apply the persistent homology analysis on the diffusion space of Monte Carlo configurations, which can essentially be understood as a dimensionality reduction of the original configuration space. In this case, we would expect that the rank of the homology group H_0, which corresponds to the number of connected clusters, would be equal to the number of topological sectors in the low temperature regime assuming a sufficient number of Monte Carlo samples, and would drop to one at the deconfinement transition, namely the point at which the sector manifolds merge.

6.2 Topological Order in Weyl Semimetals

6.2.1 Summary and Outlook for Chapter 5

In Chapter 5, we reviewed the defining property of Weyl semimetals, namely topologically protected gapless nodes hosting Weyl fermions with momentum space separation, and the resulting chiral anomaly response. Following this, we reviewed a construction for $\mathbb{Z}_4$ topological order, which involves produced a gapping a Weyl semimetal with superconducting pairing, and condensing flux 4π superconducting vortices [33]. Namely, $\Phi = n\pi$ loops for $n < 4$ survive as non-trivial gapped loop excitations, with odd flux loops possessing non-Abelian statistics and flux 2π loops possessing non-trivial Abelian statistics.

We have shown that the same topological order can be constructed from considering charge density wave interactions in a gapless Weyl semimetal. Namely, at a Weyl node separation of $2Q = \pi$, there exists two degenerate ground states corresponding to two different values of the charge density wave order parameter: $\varphi = 0, \pi$. The same $\mathbb{Z}_4$ topological order as described in [33, 34], namely odd flux vortices with non-Abelian statistics and flux 2π vortices with non-trivial Abelian statistics, can be constructed upon applying BCS pairing and flux 4π vortex condensation to the Hamiltonian for the domain wall bound states.

We have additionally computed the edge theory of the BF theory description for this topological order. The 2D surface state Lagrangian, which is obtained upon imposing a boundary on the BF theory and gauge-fixing to restore gauge invariance, appears to behave as a chiral Luttinger liquid along the x direction, since the charge propagator is shown to be $\mathcal{G}(x,t) \sim \frac{1}{(x+vt)^m}$. Ultimately, there is still much to be explored about the nature of the edge theory, including the nature of transport along the z direction. We leave this exploration for future work, noting that one possibility may be to follow the approach of L. Balents and M. Fisher, which studies the 2d chiral surface theory of a 3d quantum Hall sample using a standard renormalization group [72]. It would also be interesting to explore work done by X. Chen et al, which studies the surface theory of a $(3+1)$d BF theory with a gauged $\mathbb{Z}_2$ symmetry [73].

References

[1] D. Sehayek and R. G. Melko, "Persistent homology of $\mathbb{Z}_2$ gauge theories," 2022. arXiv:2201.09856.

[2] C. Tralie, N. Saul, and R. Bar-On, "Ripser.py: A lean persistent homology library for python," *The Journal of Open Source Software*, vol. 3, p. 925, Sep 2018.

[3] D. Sehayek, M. Thakurathi, and A. A. Burkov, "Charge density waves in weyl semimetals," *Phys. Rev. B*, vol. 102, p. 115159, Sep 2020.

[4] M. He, H. Sun, and Q. L. He, "Topological insulator: Spintronics and quantum computations," *Frontiers of Physics*, vol. 14, p. 43401, May 2019.

[5] A. Kitaev, "Periodic table for topological insulators and superconductors," *AIP Conference Proceedings*, vol. 1134, no. 1, pp. 22–30, 2009.

[6] X.-G. Wen, "Colloquium: Zoo of quantum-topological phases of matter," *Rev. Mod. Phys.*, vol. 89, p. 041004, Dec 2017.

[7] J. M. Kosterlitz and D. J. Thouless, "Ordering, metastability and phase transitions in two-dimensional systems," *Journal of Physics C: Solid State Physics*, vol. 6, pp. 1181–1203, apr 1973.

[8] C. Nayak, S. H. Simon, A. Stern, M. Freedman, and S. Das Sarma, "Non-abelian anyons and topological quantum computation," *Rev. Mod. Phys.*, vol. 80, pp. 1083–1159, Sep 2008.

[9] V. Lahtinen and J. K. Pachos, "A Short Introduction to Topological Quantum Computation," *SciPost Phys.*, vol. 3, p. 021, 2017.

[10] L. Balents, "Spin liquids in frustrated magnets," *Nature*, vol. 464, pp. 199–208, Mar 2010.

[11] Z. Chen *et al.*, "Exponential suppression of bit or phase errors with cyclic error correction," *Nature*, vol. 595, pp. 383–387, Jul 2021.

[12] K. J. Satzinger *et al.*, "Realizing topologically ordered states on a quantum processor," *Science*, vol. 374, no. 6572, pp. 1237–1241, 2021.

[13] G. Semeghini *et al.*, "Probing topological spin liquids on a programmable quantum simulator," *Science*, vol. 374, no. 6572, pp. 1242–1247, 2021.

[14] M. Levin and X.-G. Wen, "Detecting topological order in a ground state wave function," *Phys. Rev. Lett.*, vol. 96, p. 110405, Mar 2006.

[15] A. Kitaev and J. Preskill, "Topological entanglement entropy," *Phys. Rev. Lett.*, vol. 96, p. 110404, Mar 2006.

[16] A. Kitaev, "Fault-tolerant quantum computation by anyons," *Annals of Physics*, vol. 303, no. 1, pp. 2–30, 2003.

[17] M. A. Levin and X.-G. Wen, "String-net condensation: A physical mechanism for topological phases," *Phys. Rev. B*, vol. 71, p. 045110, Jan 2005.

[18] F. J. Wegner, "Duality in generalized ising models and phase transitions without local order parameters," *Journal of Mathematical Physics*, vol. 12, no. 10, pp. 2259–2272, 1971.

[19] J. B. Kogut, "An introduction to lattice gauge theory and spin systems," *Rev. Mod. Phys.*, vol. 51, pp. 659–713, Oct 1979.

[20] R. R. Coifman, S. Lafon, A. B. Lee, M. Maggioni, B. Nadler, F. Warner, and S. W. Zucker, "Geometric diffusions as a tool for harmonic analysis and structure definition of data: Diffusion maps," *Proceedings of the National Academy of Sciences*, vol. 102, no. 21, pp. 7426–7431, 2005.

[21] W. H. J. de la Porte, B. M. Herbst and S. J. van der Walt, "An introduction to diffusion maps," November 2008.

[22] J. F. Rodriguez-Nieva and M. S. Scheurer, "Identifying topological order through unsupervised machine learning," *Nature Physics*, vol. 15, pp. 790–795, Aug 2019.

[23] J. Wang, W. Zhang, T. Hua, and T.-C. Wei, "Unsupervised learning of topological phase transitions using the calinski-harabaz index," *Phys. Rev. Research*, vol. 3, p. 013074, Jan 2021.

[24] R. Ghrist, "Barcodes: The persistent topology of data," *B. Am. Math. Soc.*, vol. 45, pp. 61–75, 2008.

[25] A. Zomorodian and G. Carlsson, "Computing persistent homology," *Discrete & Computational Geometry*, vol. 33, pp. 249–274, Feb 2005.

[26] G. Carlsson, "Topology and data," *B. Am. Math. Soc.*, vol. 46, pp. 255–308, 2009.

[27] Edelsbrunner, Letscher, and Zomorodian, "Topological persistence and simplification," *Discrete & Computational Geometry*, vol. 28, pp. 511–533, Nov 2002.

[28] I. Donato, M. Gori, M. Pettini, G. Petri, S. De Nigris, R. Franzosi, and F. Vaccarino, "Persistent homology analysis of phase transitions," *Phys. Rev. E*, vol. 93, p. 052138, May 2016.

[29] Q. H. Tran, M. Chen, and Y. Hasegawa, "Topological persistence machine of phase transitions," *Phys. Rev. E*, vol. 103, p. 052127, May 2021.

[30] B. Olsthoorn, J. Hellsvik, and A. V. Balatsky, "Finding hidden order in spin models with persistent homology," *Phys. Rev. Research*, vol. 2, p. 043308, Dec 2020.

[31] A. Cole, G. J. Loges, and G. Shiu, "Quantitative and interpretable order parameters for phase transitions from persistent homology," 2020.

[32] N. Sale, J. Giansiracusa, and B. Lucini, "Quantitative analysis of phase transitions in two-dimensional xy models using persistent homology," 2021.

[33] C. Wang, L. Gioia, and A. A. Burkov, "Fractional quantum hall effect in weyl semimetals," *Phys. Rev. Lett.*, vol. 124, p. 096603, Mar 2020.

[34] M. Thakurathi and A. A. Burkov, "Theory of the fractional quantum hall effect in weyl semimetals," *Phys. Rev. B*, vol. 101, p. 235168, Jun 2020.

[35] X.-G. Wen, *Quantum Field Theory of Many-Body Systems*. Oxford University Press, 2004.

[36] D. Tong, "Lecture notes on the quantum hall effect," June 2016. University of Cambridge.

[37] J. M. Leinaas and J. Myrheim, "On the theory of identical particles," *Il Nuovo Cimento B (1971-1996)*, vol. 37, pp. 1–23, Jan. 1977.

[38] L. Savary and L. Balents, "Quantum spin liquids: a review," *Reports on Progress in Physics*, vol. 80, p. 016502, nov 2016.

[39] N. Iqbal and J. McGreevy, "Mean string field theory: Landau-ginzburg theory for 1-form symmetries," 2021. arXiv:2106.12610.

[40] J. McGreevy, "Generalized symmetries in condensed matter," 2022. arXiv:2204.03045.

[41] S. Elitzur, "Impossibility of spontaneously breaking local symmetries," *Phys. Rev. D*, vol. 12, pp. 3978–3982, Dec 1975.

[42] M. Qi, L. Radzihovsky, and M. Hermele, "Fracton phases via exotic higher-form symmetry-breaking," *Annals of Physics*, vol. 424, p. 168360, 2021.

[43] S. Sachdev, "Lecture note on the $\mathbb{Z}_2$ gauge theory," February 2018. Harvard University.

[44] R. G. Melko, "Lecture notes on quantum many-body physics," March 2016. Perimeter Institute for Theoretical Physics.

[45] L. Melas-Kyriazi, "The mathematical foundations of manifold learning," 2020. arXiv:2011.01307.

[46] H. Adams, T. Emerson, M. Kirby, R. Neville, C. Peterson, P. Shipman, S. Chepushtanova, E. Hanson, F. Motta, and L. Ziegelmeier, "Persistence images: A stable vector representation of persistent homology," *Journal of Machine Learning Research*, vol. 18, no. 8, pp. 1–35, 2017.

[47] X. G. Wen and Q. Niu, "Ground-state degeneracy of the fractional quantum hall states in the presence of a random potential and on high-genus riemann surfaces," *Phys. Rev. B*, vol. 41, pp. 9377–9396, May 1990.

[48] T. Ihn, "Lecture notes on topology in physics," 6 2018. ETH.

[49] M. V. Berry, "Quantal phase factors accompanying adiabatic changes," *Proceedings of the Royal Society of London. A. Mathematical and Physical Sciences*, vol. 392, no. 1802, pp. 45–57, 1984.

[50] N. P. Armitage, E. J. Mele, and A. Vishwanath, "Weyl and dirac semimetals in three-dimensional solids," *Rev. Mod. Phys.*, vol. 90, p. 015001, 1 2018.

[51] A. A. Burkov, "Chiral anomaly and transport in weyl metals," *Journal of Physics: Condensed Matter*, vol. 27, p. 113201, 2 2015.

[52] A. Burkov, "Weyl metals," *Annual Review of Condensed Matter Physics*, vol. 9, no. 1, pp. 359–378, 2018.

[53] A. A. Burkov and L. Balents, "Weyl semimetal in a topological insulator multilayer," *Phys. Rev. Lett.*, vol. 107, p. 127205, Sep 2011.

[54] T. M. McCormick, I. Kimchi, and N. Trivedi, "Minimal models for topological weyl semimetals," *Phys. Rev. B*, vol. 95, p. 075133, Feb 2017.

[55] S. Florens and A. Georges, "Slave-rotor mean-field theories of strongly correlated systems and the mott transition in finite dimensions," *Phys. Rev. B*, vol. 70, p. 035114, Jul 2004.

[56] S.-S. Lee and P. A. Lee, "U(1) gauge theory of the hubbard model: Spin liquid states and possible application to $\kappa-(\mathrm{BEDT-TTF})_2\mathrm{cu}_2(\mathrm{CN})_3$," *Phys. Rev. Lett.*, vol. 95, p. 036403, Jul 2005.

[57] A. A. Burkov, "Dirac fermion duality and the parity anomaly," *Phys. Rev. B*, vol. 99, p. 035124, Jan 2019.

[58] G. Bednik, A. A. Zyuzin, and A. A. Burkov, "Superconductivity in weyl metals," *Phys. Rev. B*, vol. 92, p. 035153, Jul 2015.

[59] T. Meng and L. Balents, "Weyl superconductors," *Phys. Rev. B*, vol. 86, p. 054504, Aug 2012.

[60] Villain, J., "Theory of one- and two-dimensional magnets with an easy magnetization plane. ii. the planar, classical, two-dimensional magnet," *J. Phys. France*, vol. 36, no. 6, pp. 581–590, 1975.

[61] O. I. Motrunich and T. Senthil, "Origin of artificial electrodynamics in three-dimensional bosonic models," *Phys. Rev. B*, vol. 71, p. 125102, Mar 2005.

[62] Z. Wang and S.-C. Zhang, "Chiral anomaly, charge density waves, and axion strings from weyl semimetals," *Phys. Rev. B*, vol. 87, p. 161107, Apr 2013.

[63] A. Decelle, V. Martin-Mayor, and B. Seoane, "Learning a local symmetry with neural networks," *Phys. Rev. E*, vol. 100, p. 050102, Nov 2019.

[64] D. Lozano-Gómez, D. Pereira, and M. J. P. Gingras, "Unsupervised machine learning of quenched gauge symmetries: A proof-of-concept demonstration," 2020. arXiv: 2003.00039.

[65] J. Jia and W. Wang, "Review of reinforcement learning research," in *2020 35th Youth Academic Annual Conference of Chinese Association of Automation (YAC)*, pp. 186–191, 2020.

[66] K. Arulkumaran, M. P. Deisenroth, M. Brundage, and A. A. Bharath, "Deep reinforcement learning: A brief survey," *IEEE Signal Processing Magazine*, vol. 34, no. 6, pp. 26–38, 2017.

[67] I. S. Tupitsyn, A. Kitaev, N. V. Prokof'ev, and P. C. E. Stamp, "Topological multicritical point in the phase diagram of the toric code model and three-dimensional lattice gauge higgs model," *Phys. Rev. B*, vol. 82, p. 085114, Aug 2010.

[68] A. M. Somoza, P. Serna, and A. Nahum, "Self-dual criticality in three-dimensional $\mathbb{Z}_2$ gauge theory with matter," 2020.

[69] T. Kennedy and H. Tasaki, "Hidden $z_2 \times z_2$ symmetry breaking in haldane-gap antiferromagnets," *Phys. Rev. B*, vol. 45, pp. 304–307, Jan 1992.

[70] M. den Nijs and K. Rommelse, "Preroughening transitions in crystal surfaces and valence-bond phases in quantum spin chains," *Phys. Rev. B*, vol. 40, pp. 4709–4734, Sep 1989.

[71] M. Dupont, S. Gazit, and T. Scaffidi, "Evidence for deconfined $u(1)$ gauge theory at the transition between toric code and double semion," *Phys. Rev. B*, vol. 103, p. L140412, Apr 2021.

[72] L. Balents and M. P. A. Fisher, "Chiral surface states in the bulk quantum hall effect," *Phys. Rev. Lett.*, vol. 76, pp. 2782–2785, Apr 1996.

[73] X. Chen, A. Tiwari, C. Nayak, and S. Ryu, "Gauging (3+1)-dimensional topological phases: An approach from surface theories," *Phys. Rev. B*, vol. 96, p. 165112, Oct 2017.

[74] L. D. Landau, "On the theory of phase transitions. I.," *Phys. Z. Sowjet.*, vol. 11, p. 26, 1937.

[75] N. Read and S. Sachdev, "Large-n expansion for frustrated quantum antiferromagnets," *Phys. Rev. Lett.*, vol. 66, pp. 1773–1776, Apr 1991.

[76] X. G. Wen, "Mean-field theory of spin-liquid states with finite energy gap and topological orders," *Phys. Rev. B*, vol. 44, pp. 2664–2672, Aug 1991.

[77] M. Freedman, C. Nayak, K. Shtengel, K. Walker, and Z. Wang, "A class of p,t-invariant topological phases of interacting electrons," *Annals of Physics*, vol. 310, no. 2, pp. 428–492, 2004.

[78] J. McGreevy, "Lecture notes in topology from physics," May 2021. University of California at San Diego.

[79] J. Knolle and R. Moessner, "A field guide to spin liquids," *Annual Review of Condensed Matter Physics*, vol. 10, no. 1, pp. 451–472, 2019.

[80] J. Carrasquilla and R. G. Melko, "Machine learning phases of matter," *Nature Physics*, vol. 13, pp. 431–434, May 2017.

[81] Y. Zhang and E.-A. Kim, "Quantum loop topography for machine learning," *Phys. Rev. Lett.*, vol. 118, p. 216401, May 2017.

[82] V. S. Dotsenko, P. Windey, G. Harris, E. Marinari, E. Martinec, and M. Picco, "Critical and topological properties of cluster boundaries in the 3d ising model," *Phys. Rev. Lett.*, vol. 71, pp. 811–814, Aug 1993.

[83] V. S. Dotsenko, G. Harris, E. Marinari, E. Martinec, M. Picco, and P. Windey, "The phenomenology of strings and clusters in the 3-d ising model," 1994. arXiv:hep-th/9401129.

[84] D. Sehayek, M. Thakurathi, and A. A. Burkov, "Charge density waves in weyl semimetals," *Phys. Rev. B*, vol. 102, p. 115159, Sep 2020.

[85] T. Senthil, "Symmetry-protected topological phases of quantum matter," *Annual Review of Condensed Matter Physics*, vol. 6, no. 1, pp. 299–324, 2015.